

**Analysis of Low-Noise EEG
in Search of Functional Gamma Band Correlates**

by

Nazanin Hamzei

B.Sc., Amirkabir University of Technology, 2012

A THESIS SUBMITTED IN PARTIAL FULFILLMENT
OF THE REQUIREMENTS FOR THE DEGREE OF

Master of Applied Science

in

THE FACULTY OF GRADUATE AND POSTDOCTORAL STUDIES
(Electrical and Computer Engineering)

The University Of British Columbia
(Vancouver)

April 2017

© Nazanin Hamzei, 2017

Abstract

The electroencephalogram (EEG) has proven to be a useful information source in analysis of brain activity, diagnosis of neurological disorders, and development of brain-computer interfaces (BCI's). Through numerous studies over the past decades, EEG activity in different frequency bands has been observed to correspond with various mental states. Clinical use of EEG, however, is often limited to frequency ranges below 30 *Hz*, ignoring potentially informative patterns within the gamma band (30 – 100 *Hz*). Indeed, the gamma band has received greater scrutiny in recent years and is typically known to underlie and be modulated by sensorimotor behaviors and internal cognitive processes.

In this study, we have investigated the potential of an ultra-low noise capsule at the LSBB¹ for acquisition of clean EEG signals, with a focus on analysis of high frequencies (gamma band) in search for novel activity patterns. Using a battery-operated EEG acquisition system, we acquired 64-channel EEG recordings from a few volunteers performing several cognitive, sensory, and motor tasks in both LSBB and a typical research laboratory. Upon analysis of this data using Stockwell Transform, we compared task-specific gamma band energy increases of signals acquired at the two environments, observing more prominent functional EEG changes in LSBB. Moreover, we studied all recordings in both environments to examine statistically significant spatial and spectral correlates of spontaneous EEG pertaining to each of the tasks.

To further assess the task-induced changes in the EEG signals, we have also proposed a framework for analyzing gamma band connectivity; i.e. functional patterns of interaction between distinct channels of the EEG. Using this framework,

¹Laboratoire Souterrain à Bas Bruit, Rustrel, France

we have analyzed directional connectivity on recordings pertaining to motor tasks, both in a batch-based (yielding a time-averaged pattern) and an instantaneous manner. Batch-based connectivity analysis of the data resulted in well-defined connectivity patterns among subjects, while instantaneous connectivity analysis was inconsistent due to limitations of the study protocol. The results obtained in this thesis demonstrate the potential of the low-noise capsule and motivate further protocol enhancements and analysis methods for conducting high-frequency EEG studies at LSBB.

Preface

This dissertation is the original work of the author in collaboration with the Electrical and Computer Engineering in Medicine (ECEM) research group at the University of British Columbia. The principal investigator, professor Guy A Dumont, was responsible for design of the experimental paradigm, recruitment of subjects (all of whom are interested researchers known to the principal investigator), and collection of data, as approved by the UBC Research Ethics Board (certificate number H14-02124, August 2014). The author was solely involved in concept formation and data analysis.

The following article has been published out of the context of the work in section 2.3.2:

- Hamzei, N., Bastany, Z., Jutzeler, C.R., Yedlin, M., Kramer, J.L., Steeves, J.D. and Dumont, G.A., 2016. Ultra-low Noise EEG at LSBB: New results. In *E3S Web of Conferences* (Vol. 12, p. 05003). EDP Sciences.

Additionally, the following articles will be written and submitted based on the framework laid out in this thesis:

- *High-frequency correlates of spontaneous EEG in response to cognitive and sensorimotor tasks*
- *Topographical analysis of spontaneous Granger-causal connectivity during movement-related tasks: an EEG study*

Table of Contents

Abstract	ii
Preface	iv
Table of Contents	v
List of Tables	viii
List of Figures	ix
List of Abbreviations	xi
Acknowledgements	xii
1 Introduction	1
1.1 Background And Basics of Electroencephalography	1
1.2 EEG Signal Analysis	2
1.2.1 EEG Patterns And Brain Waves	2
1.2.2 General Review of Analysis Techniques	6
1.3 Thesis Objectives	7
1.3.1 Contributions	9
2 Time-frequency Analysis Using Stockwell Transform	11
2.1 Introduction	11
2.2 Data Preparation	13
2.2.1 Artifact Rejection	13

2.2.2	Pre-processing	17
2.3	Data Analysis	19
2.3.1	Stockwell Transform	19
2.3.2	Comparison of the Two Environments	22
2.3.3	Task-specific EEG Changes in Both Environments	28
2.4	Discussion And Conclusions	37
3	Granger-Causal Connectivity Analysis	39
3.1	Introduction	39
3.1.1	Motivation for Connectivity Analysis	39
3.1.2	Different Categories of Connectivity	40
3.1.3	Modeling And Estimation of Connectivity	41
3.2	Theory	43
3.2.1	Granger Causality	43
3.2.2	MultiVariate AutoRegressive (MVAR) Models	44
3.2.3	Autoregressive Modeling of Nonstationary Data	45
3.2.4	Representation in Frequency Domain	46
3.2.5	Frequency Domain Estimators of Directed Connectivity	47
3.3	Workflow, Methods, And Practical Considerations	50
3.3.1	Pre-processing And Artifact Removal	50
3.3.2	Model Fitting And Validation	52
3.3.3	Computation of Connectivity Estimators	55
3.3.4	Tests for Statistical Significance	56
3.3.5	Visualization and Further Data Reduction	58
3.4	Results And Discussion	62
3.4.1	Static Connectivity Results	64
3.4.2	Dynamic Connectivity Results	71
3.4.3	Conclusion	74
4	Conclusion	76
4.1	Summary	76
4.2	Limitations	77
4.3	Future Work	78

Bibliography	80
A Details of the Study	91
A.1 The Underground Facility	91
A.2 Acquisition System	91
A.3 Study Protocol	92

List of Tables

Table 2.1	Grouping of the electrodes in a 10-10 montage based on their locations	24
Table 2.2	Different frequency bands used in our analysis.	29

List of Figures

Figure 1.1	EEG electrode placement in the international 10-20 system. . .	3
Figure 1.2	EEG decomposition into standard subbands	4
Figure 2.1	ICA decomposition of a noisy segment of EEG	15
Figure 2.2	Stockwell transform magnitude of resting state as well as that of a motor task at LSBB	21
Figure 2.3	Stockwell transform magnitude of resting state as well as that of a motor task at both LSBB and ICORD	23
Figure 2.4	Topographical map of electrode groups based on the classifi- cation in Table 2.1	24
Figure 2.5	Box plots demonstrating the distribution of energy ratios across subjects in different brain regions, conditions, and environments.	26
Figure 2.6	Significance maps and Power Change Ratios of the backward counting task	31
Figure 2.7	Significance maps and Power Change Ratios of the matching memory task	32
Figure 2.8	Significance maps and Power Change Ratios of the brushing task	33
Figure 2.9	Significance maps and Power Change Ratios during the appli- cation of hot packs	34
Figure 2.10	Significance maps and Power Change Ratios of the ankle move- ment task	35
Figure 2.11	Significance maps and Power Change Ratios of the wrist move- ment task	36

Figure 3.1	From raw time series to connectivity patterns: steps for estimating effective connectivity based on multivariate autoregressive models	51
Figure 3.2	Normalized auto and cross-correlations among all 60 channels of the model residuals	54
Figure 3.3	Statistical significance testing methods for pair-wise static and dynamic connectivity estimation	57
Figure 3.4	Visualization of the connectivity structure by plotting the significance matrix	59
Figure 3.5	Visualization of significant interactions by averaging channel interactions within the brain regions specified in table 2.1. . .	60
Figure 3.6	Representation of brain networks as graphs	61
Figure 3.7	Significant directed pair-wise connections during ankle movement from three subjects in the two environments	65
Figure 3.8	Segmentation of significance matrices into hemispheric connections	66
Figure 3.9	Overall strengths of inter and intra-hemispheric task-specific connectivity during motor tasks	66
Figure 3.10	Average regional interactions during motor tasks in eight subjects and two environments.	68
Figure 3.11	Topographical plots showing the static graph-theoretical measures calculated on the mean significance matrix during motor tasks	70
Figure 3.12	Topographical plots of instantaneous CAR values during the first five seconds of ankle movement	72
Figure 3.13	Time course of gamma band interactions throughout the first five seconds of ankle movement from one subject at LSBB . .	73
Figure A.1	EEG montage of the NRSig acquisition system	92

List of Abbreviations

EEG	Electroencephalogram
LSBB	Laboratoire Souterrain à Bas Bruit
ICORD	International Collaboration On Repair Discoveries
BCI	Brain-Computer Interface
FMRI	functional Magnetic Resonance Imaging
ERP	Event-Related Potentials
STFT	Short-Time Fourier Transform
WT	Wavelet Transform
ICA	Independent Component Analysis
DDTF	direct Directed Transfer Function
VAS	Visual Analog Scale
PCR	Power Change Ratio
CNS	Central Nervous System
MVAR	MultiVariate AutoRegressive
CAR	Causal Asymmetry Ratio

Acknowledgements

My gratitude goes out to my academic supervisor, professor Guy Dumont, for his insightfulness, professionalism, generosity, and unwavering support throughout this process. I would also like to thank Dr. John Kramer, Dr. John Steeves, Dr. Matthew Yedlin, Ms. Zoya Bastani, and Mr. Shahbaz Askari for their helpful and encouraging comments on this work.

My sincere gratitude extends to my parents for all the sacrifices they made to support my aspirations. I am also indebted to my partner, Mahdi, who listened patiently to my occasional rants, set me straight at times when I staggered, and stayed lovingly by my side along the way.

Chapter 1

Introduction

1.1 Background And Basics of Electroencephalography

In 1924, psychiatrist Hans Berger's obsession with understanding the "psychic energy" led to one of the most remarkable developments in the history of neurology. His paper was published five years later, demonstrating that the electrical activity of the human brain can be recorded from the surface of the scalp. Using his method, later known as electroencephalography (EEG), he was the first to study changes in the recorded EEG signal pertaining to specific mental processes, including arousal, memory, and consciousness. Application of EEG in detection of epilepsy followed not long after, when Gibbs et al. discovered the spike-and-wave discharge as a first-ever clear EEG pattern particular to petit mal epilepsy [1]. Nowadays, EEG continues to be a valuable research and diagnosis tool in neurophysiology, with applications ranging from diagnosis of brain injuries and mental disorders [2] to monitoring the depth of anesthesia in the operating room [3] and design of sophisticated Brain-Computer Interfaces (BCI's) [4].

The physiological basis of brain's electrical activity lies in that the core components of the central nervous system, i.e. neurons, have intrinsic electrical properties. Neurons are electrically excitable cells capable of being activated by other neurons through afferent electrochemical action potentials [5]. EEG is therefore hypothesized to comprise of the summed electrical activities (net electric field) of these post-synaptic potentials. A large cluster of synchronously activated neurons

are involved in generation of EEG, which is then propagated to the scalp surface. Passing through many layers before reaching the scalp, this signal is severely attenuated; and hence only large populations (thousands to millions) of neurons with coherent orientations of electric fields can generate enough potential to be recordable using scalp electrodes.

The EEG acquisition system is relatively simple and inexpensive compared to neuroimaging devices. It mainly comprises of electrodes distributed over the scalp in a standard and reproducible placement scheme (e.g. in the international 10-20 montage shown in figure 1.1, the electrodes are placed at intervals which are 10% and 20% of the total front-back and left-right distance of the skull, respectively). Held in place on the scalp using conductive pastes, caps, or nets, each electrode is connected to one input of a differential amplifier, with the other input connected to a reference electrode. The signal picked up on the scalp surface is amplified, digitized and sampled, typically at sampling frequencies greater than 256 *Hz*, thus providing a millisecond-range temporal resolution. Compared to other tools for exploring neural activity such as FMRI, this high temporal resolution is another attractive feature of EEG which provides the opportunity of studying brain function in real time.

1.2 EEG Signal Analysis

EEG traces recorded over time contain information about the brain state or potential neural disorders. Clinical professionals with a trained eye typically obtain this information by visual inspection of the time series. However, multichannel EEG is a highly complex signal in nature, holding many potentially valuable features which cannot be visually discerned. The purpose of the current trend of research on quantitative EEG signal analysis is, therefore, to extend and apply the concepts of digital signal processing to the analysis of EEG to make use of this rich information source as a low-cost and non-invasive 'window to the brain'.

1.2.1 EEG Patterns And Brain Waves

Depending on the application, the patterns sought after in EEG are either rhythmic activity or transients. Transient features of the signal, such as occurrence of spikes

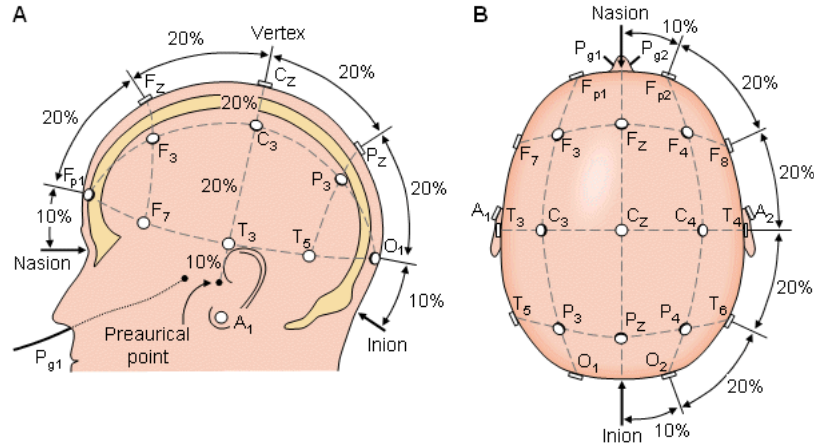


Figure 1.1: EEG electrode placement in the international 10-20 system. There are a total of 19 recording electrodes spanned uniformly from front to back of the head (nasion to inion) and from left to right (between pre-auricular points). Additionally, two reference electrodes (often placed on ear lobes) and one or two ground electrodes (often placed on the nose) are included. Electrode names refer to their corresponding location, with F, C, P, T, and O denoting Frontal, Central, Parietal, Temporal, and Occipital lobes, respectively. A) side view, B) top view.

and sharp waves (SSW), may represent seizures or interictal activity [6]. On the other hand, rhythmic oscillations, or the so-called notion of *brain waves*, refer to the relative signal content within different frequency bands in the EEG spectrum (Figure 1.2). Conventionally, rhythmic activity of EEG is studied in a number of specific and standard frequency bands, including *delta* (0.1 – 4Hz), *theta* (4 – 8Hz), *alpha* (8 – 12Hz), *beta* (12 – 30Hz), and *gamma* (30 – 100Hz). These distinctive categories are sometimes noted to have a certain spatial distribution over the scalp and are often attributed to certain biophysical correlates such as particular brain states [7]. The low-frequency, high-amplitude delta waves ($< 4\text{ Hz}$) are a primary indicator of deep sleep in adults and the predominant activity in infants during the first two years of life, while hippocampal theta waves ($\sim 4 - 8\text{ Hz}$) have been associated with drowsiness and deep meditation. Alpha oscillations (8 – 12Hz) are largest in the posterior regions of the brain and have been associated

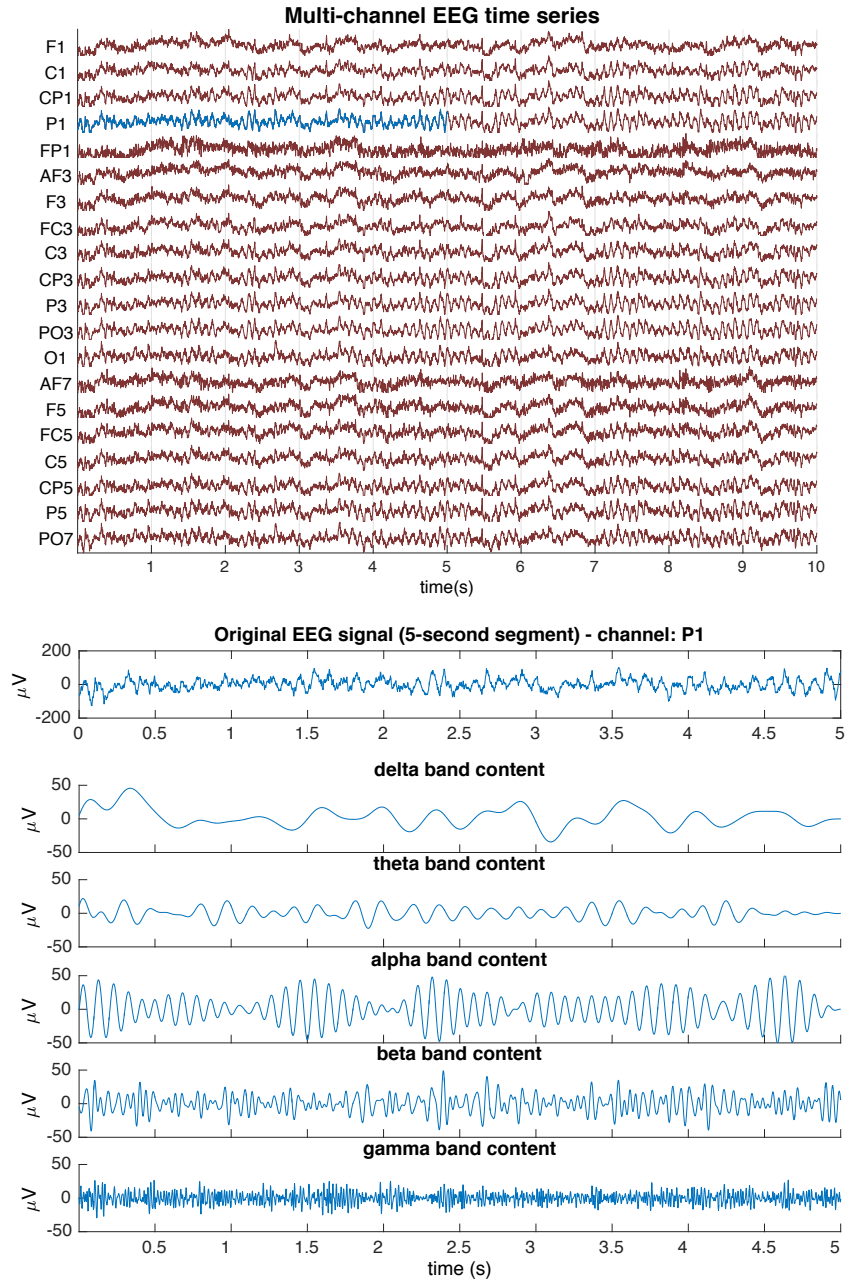


Figure 1.2: Top: typical 10 second-length multichannel EEG time series; labels on the vertical axis indicate channel names (chosen arbitrarily from a 10-10 montage). Bottom: first 5 seconds of the P1 signal filtered into its corresponding standard sub-bands.

with relaxed wakefulness with eyes closed. Oscillations in the 12 – 30 *Hz* range are generally smaller in amplitude compared to lower frequency waves, and are known as beta oscillations. These rhythms are distributed symmetrically on the fronto-central regions and are associated with active thinking and focused attention [5].

Gamma band oscillations, earlier defined as narrow-band 40 *Hz* waves and later modified to the 30 – 100 *Hz* (and above) range, deserve more attention as they have been the subject of many EEG studies (including this thesis) during the past decades. These studies, however, typically lead to controversies. This is due to the fact that gamma band activity is observed in a multiplicity of cognitive processes, but it is not unique to any of these functions and is hence not regarded as a strict indicator of these processes [8]. Since the late nineteen-eighties, gamma band has been linked to perceptual binding, i.e. the ability of the brain to fuse various aspects of a stimulus into a coherent whole [9], [8], [5]. Later on, gamma band oscillations were also associated with many other cognitive functions such as attention [10], arousal and alertness [11], perception and memory [12], [13], language processing [14], top-down modulation of sensory processes [15], movement-related tasks [16], and pain processing [17]. Nonetheless, a somewhat general explanatory theory regarding the gamma band does not exist and the role of gamma band in cognitive and sensorimotor processing is yet to be elucidated.

Based on different activation patterns of gamma waves, Galambos [18] suggested the following categories for classification of studies on gamma band:

1. **Spontaneous** gamma oscillations, which are essentially ongoing (background) gamma band activity in EEG without intentional stimulation; and can be defined at all times as the fraction of power in the gamma band in relation to the total signal power.
2. **Induced** gamma waves, which are caused by but not specifically time-locked to a stimulus. The induced gamma responses usually occur at post-stimulus latencies longer than 100 milliseconds and usually less than a second, and may vary in latency from trial to trial. This kind of activity is the subject of the majority of gamma band studies in the literature.
3. The **evoked** gamma responses, on the other hand, are precisely time-locked

to the stimulus, with post-stimulus latencies usually around 25 milliseconds.

4. The **emitted** gamma band oscillations, occurring in cases when there is a response time-locked to a stimulus which is not presented. This might happen in paradigms when the subject is expecting a stimulus at a specific point in time, but is not presented with any.

Contrary to Galambos' classification in 1992, the current literature on gamma band makes loose distinctions between the terminology of induced, evoked, or emitted responses. However, it seems natural and essential to distinguish continuous spontaneous activity from transient time-locked responses caused by a stimulus. While very few studies have focused on the former (usually in the realm of sleep stages), the latter responses are studied extensively in the past decades. In fact, most of the studies on EEG oscillations focus on establishment of trial-averaged Event-Related Potentials (ERP's) as physiological correlates of cognitive, sensory, and perceptual phenomena.

1.2.2 General Review of Analysis Techniques

Numerous methods and techniques developed in electrical engineering and information theory have been utilized over the past decades to augment the power of analysis of EEG signals (See [19], [20], [21] for a review on these methods). The main goal of all of these methods is to quantify and correlate changes observed in the EEG signal with the underlying mental process or disorder which is believed to cause these changes. The methods range from time domain analysis, such as Hjorth's trio of descriptive statistics parameters [22], [23]; to parametric and non-parametric frequency domain (spectral analysis) methods [24], [25]; as well as time-frequency methods and the use of wavelet and short-time Fourier transforms [26], [27], [28], [29] to determine *when* specific spectral events happen in the EEG. On the other hand, non-linear signal processing methods such as mutual information studies [30], higher order spectral [31], [32], fractal [33], [34], and entropy analysis methods [35], [36] have also been explored and used on EEG signals.

There have been numerous attempts to solve the EEG inverse problem; namely, reconstructing the sources hypothesized to give rise to scalp signals [37], [38]. In this context, the scalp signals are assumed to be projected mixtures of an infi-

nite number of cortical sources at different locations within the brain. Hence, by solving the inverse problem, one would be able to examine the source domain as opposed to the sensor (electrode) domain to have a more refined localization of activity patterns. This is of particular interest when scalp EEG is being used as a non-invasive tool to localize interictal spikes characteristic of epilepsy. Dipole source localization methods [39], minimum-norm solutions [40], Low-resolution Electromagnetic Tomography (LORETA) [41], Bayesian solutions [42], and Independent Component Analysis (ICA) [43] are among the popular source estimation techniques found in literature.

From another perspective, many neuro-scientific publications during the past few years have shifted their focus from segregated functional localization to functional connectivity analysis [44], [45], [46], [47], [48]. Specifically, it is now commonly accepted that during information processing, the brain is not merely structured in separate, isolated parts. Rather, it behaves as a complex network of different, possibly distant regions interacting with each other in various ways. Research in brain connectivity therefore refers to application of signal processing techniques to quantify the information exchanged between different regions of the brain in different states, tasks, or disorders; in order to shed some light on the brain's complex network structure. Connectivity estimation techniques range from simple coherence analyses to more sophisticated Dynamic Causal Models [49], Structural Equation Models [50], and Multivariate Autoregressive-based models [44], [51].

1.3 Thesis Objectives

With the end goal of performing innovative EEG studies and establishment of novel low-noise EEG benchmarks, our study was designed to make use of the unique underground laboratory (**LSBB**); an ultrashielded, ultra-low noise capsule used as a cross-disciplinary research facility for low-noise measurements (See Appendix A). We have collected high-resolution continuous EEG data from a number of subjects both in LSBB and in a typical research laboratory environment, **ICORD**¹, while

¹International Collaboration On Repair Discoveries, Blusson Spinal Cord Centre, Vancouver, BC

they performed several cognitive, sensory, and motor tasks. The main objective of this work is to analyze this data in search of task-specific EEG activity patterns, with a particular emphasis on gamma band oscillations. We attempt to find functional gamma band patterns in the subjects' EEG which would correlate with the subject performing a task, and could thus serve as functional biomarkers. We also intend to see how these patterns are different in the low-noise LSBB as compared to a typical noisy environment.

The potential of the LSBB capsule for performing low-noise EEG measurements was previously assessed in a preliminary study [52], in which it was confirmed that clean EEG signals can be acquired at LSBB without the need for notch filtering. It was also shown that the battery-operated acquisition equipment does not introduce electromagnetic noise on the acquired signals. Moreover, due to higher signal-to-noise ratio, task-specific EEG biomarkers at beta band were found to be more prominent in signals acquired at LSBB compared to the hospital environment [52]. However, this preliminary study bore a number of limitations. First, the EEG system used was a clinical depth of hypnosis monitor designed for use in the operating room and only offered two EEG channels. Further, as it was a feasibility study, the experiments were not specifically designed to target functions involving gamma band oscillations. Our study was an attempt to overcome these limitations by upgrading the acquisition equipment to a 60-channel research-grade system, as well as improving the design of experiments by including a variety of tasks in which gamma band is deemed to play a role. Details of the acquisition system, environments, and the study protocol are discussed in Appendix A.

In more specific terms, the objectives of this thesis are twofold:

1. To examine the task-specific gamma band content of the data in the time-frequency domain using Stockwell Transform (S-Transform) [53]. The S-Transform is an extension of the wavelet transform with properties which make it a suitable tool for analysis of high-frequency content in a signal. Using this tool, we have attempted to identify channels (brain regions) which are actively generating gamma band activity when a particular task is being performed; and observed how these activity patterns differ across subjects. Moreover, we have used the S-Transform to compare task-specific gamma

band activity in data recorded at LSBB with those recorded in ICORD. The end goal in this comparison is to search for EEG information, particularly within the gamma band, which is conspicuously present in LSBB but not in the hospital environment and will lead us to better detection of task-specific bio-markers.

2. To analyze the task-specific effective connectivity patterns in the data in search of significant functional interactions among brain regions within the gamma band. Based on our observation from segregated time-frequency analysis, we will proceed with analyzing motor tasks, as the most consistent functional gamma band power increases were observed during these tasks. We have adopted two approaches for analyzing effective connectivity in our non-stationary EEG data. One is to analyze connectivity in non-overlapping windows (batches) and the other is to compute instantaneous connectivity parameters using an adaptive model.

These objectives are addressed individually in chapters 2 and 3, respectively. Lastly, we have summarized our findings as well as outlined the major challenges, limitations of the dataset, and directions of future work in chapter 4.

1.3.1 Contributions

Recapitulating, this work has made the following basic contributions:

- The Stockwell transform was used for time-frequency analysis on this dataset,
- Task-relevant gamma band energy increases were assessed and compared across subjects and brain regions between LSBB and the hospital environment,
- A pipeline for analysis of static (batch-averaged) and dynamic (instantaneous) effective connectivity patterns is proposed for this dataset,
- A multi-subject statistical inference scheme is proposed for group assessment of functional changes in EEG; both for time-frequency as well as static and dynamic connectivity analysis,

- The direct Directed Transfer Function (DDTF), a multivariate measure of connectivity based on parametric auto-regressive modeling of EEG, was used to measure batch-based connectivity in this dataset,
- A Recursive Least Squares algorithm with forgetting factor, coupled with DDTF, was used to extend the batch-based analysis and adaptively model instantaneous connectivity in this dataset.

Chapter 2

Time-frequency Analysis Using Stockwell Transform

2.1 Introduction

Frequency analysis of the EEG signal goes back to when EEG was discovered by Berger in 1929. He was the first to study changes in oscillatory behavior of the EEG which were present in both normal and abnormal brains. Specifically, he reported on oscillations with frequencies near 10 *Hz*, later termed as alpha waves; and their substitution by the faster oscillating beta waves when the subject opened their eyes [54]. Following Berger's pioneering work, and especially since the introduction of digital recordings and the Fast Fourier Transform, researchers have thoroughly studied different EEG oscillation patterns and their correlation to various mental states, brain functions, and pathologies.

Most studies of scalp EEG are concerned with measures on averages of responses evoked by (precisely time-locked to) a stimulus presented in a series of similar trials or epochs. It is assumed that by averaging multiple realizations of the process, background EEG and other sources of noise would be canceled out and what remains is the coherent time-and-phase-locked activity evoked by the stimulus, or the so-called Event-Related Potential (ERP). ERP's are therefore brief (generally less than 1 second), transient waves believed to represent the mental process of responding to a stimulus. Analysis of the EEG based on Event-Related Poten-

tials has a number of advantages. First, ERP's are conceptually simple and fast and easy to implement with very few analysis parameters or assumptions. These stimulus-locked brain responses can be precisely characterized by means of amplitude and latency. Also, there is an extensive and decades-long ERP literature which can be used for validation and sanity check of the experimental conditions. For instance, the P300, a component elicited at latencies close to 300 milliseconds, is a well-established ERP component in neuroscience which reliably arises in oddball paradigms [55].

The downside to the ERP approach is that responses are not necessarily stable across trials, and averaging will remove any phase-incoherent activity not precisely time-locked to the event, including potentially informative EEG activity which is roughly time-locked but not phase-locked to the stimulus onset (i.e. induced activity). To characterize changes in the ongoing EEG induced by a stimulus, Pfurtscheller introduced Event-Related Synchronization (ERS) and Event-Related Desynchronization (ERD) [56] which represent short-lasting amplitude increases and decreases of rhythmic activity, respectively. Examples of ERS are the beta rebound after limb movement [57] and the induced gamma activity during visual processing [58]. It is important to stress here that both ERD and ERS measure induced changes in EEG oscillatory activity occurring shortly (a few seconds) before or after a stimulus, focusing on the time-locked mechanisms of cortical processing.

On the other hand, a smaller portion of EEG studies, particularly studies on sleep patterns, analyze mean changes of spontaneous EEG power under various conditions. In this type of analysis, the focus is not on transient dynamics of spectral properties in the temporal vicinity of a stimulus; rather, it is on overall spectral differences in ongoing oscillatory behavior between different states or groups of pathologically different subjects. Our study falls into this category of spectral analysis due to the nature of the experiment design. The main objective in this chapter is to find changes in oscillatory behavior which are specific to performing a task, and are manifested in the EEG by consequent regional power increases (or decreases) in specific frequency bands.

Our dataset consists of approximately 5 hours of continuous EEG data recorded in two environments: 1) The low-noise underground laboratory (LSBB), and 2) a research facility (ICORD). Using a battery-operated 60-channel acquisition sys-

tem, we have recorded the EEG while subjects performed a variety of cognitive and sensorimotor tasks. The cognitive tasks included backward counting from a large number, and an increasingly challenging 'matching' memory task on an iPad. In the sensory stimulation phase, the subjects' right thumb was brushed with a cotton swab as a tactile stimulation, and the subjects were asked to hold a hot pack in their right hand as a noxious stimulus, while rating their pain experience using a visual analog scale. Finally, as motor tasks, the subjects performed flexion movements of the right ankle and the right wrist in separate sessions. Five subjects had volunteered for data acquisition at ICORD, while seven subjects were present at LSBB, four of whom were common to both environments (see Appendix A for more details on the protocol, acquisition system, and the underground environment).

As our data analysis pipeline, we first clean the data of artifacts by removing contaminated channels and rejecting artifactual time segments. We demonstrate in section 2.2.1 that for artifact rejection, ICA does not work effectively on our data and we will henceforth resort to visual inspection to clean data of artifacts. Next, we introduce the theory and justify our use of the S-Transform in section 2.3.1. We then compare the task-to-rest S-transform energy ratios in ICORD and LSBB in section 2.3.2. Next, in section 2.3.3, we merge the data in the two environments to increase our sample size and use the same S-Transform information in hopes to find consistent task-specific gamma band activity patterns across all subjects participating in the study. Lastly, we conclude and elaborate on our findings in section 2.4.

2.2 Data Preparation

2.2.1 Artifact Rejection

EEG Artifacts

Scalp EEG is almost always contaminated by noise and various artifacts which obscure potentially informative cortical activity patterns. These sources of interference are typically classified into physiological and extra-physiological artifacts. The latter refers to sources of noise and interference from the recording environ-

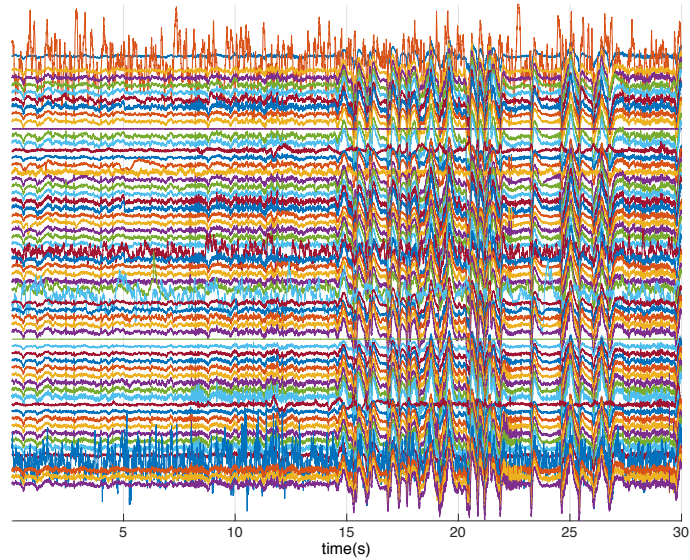
ment, including but not limited to poor electrical grounding, poor electrode contact, and powerline interference [5]. Extra-physiological artifacts can generally be mitigated by proper electrode attachment and recording the data in a controlled environment.

Physiological artifacts, on the other hand, are the main sources of contamination of the EEG signal and the main focus of studies on artifact rejection. They originate from inherent bio-physiological processes irrelevant to the EEG, and therefore can rarely be avoided. The most prevalent physiological contaminants of the EEG are subject's movements, cardiac activity or the electrocardiogram (ECG), the electromyogram (EMG) artifact caused by contraction of the muscles, and the electrooculogram (EOG) artifacts caused by blinks and eye movements [59].

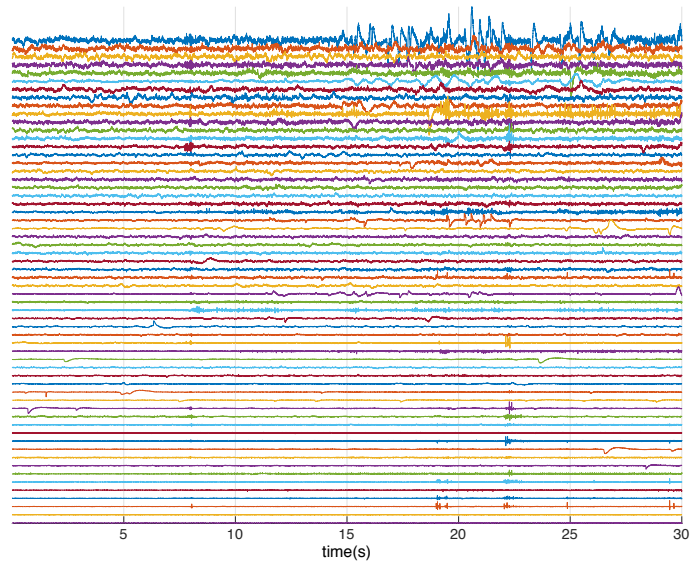
Irrespective of their cause, the artifacts distort the signal and need to be eliminated prior to quantitative analysis of EEG. Artifact suppression is typically performed by means of offline processing methods; a simple, classical example being filtering. For instance, notch filtering is often performed to remove the 50/60 Hz powerline interference and its harmonics, and high-frequency noise is eliminated by means of lowpass filtering. However, the majority of artifacts overlap in frequency content with the desired background EEG, and hence cannot be removed by bandpass filtering. Therefore, alternative techniques are typically developed, such as adaptive filtering [60], blind source separation (BSS) methods including Independent Component Analysis (ICA) [61] and Signal-Space Projection [62], or wavelet methods [63].

The ICA Method

One particularly popular artifact rejection technique in the EEG literature is Independent Component Analysis (ICA), which is an information-theoretical method for decomposition of a mixture of signals into additive subcomponents, such that these components are maximally independent at all times [64]. Essentially, ICA finds a set of fixed spatial filters which together perform a linear change of basis from the sensor domain to the so-called 'virtual channel' (component) domain. Using this approach, locally coherent activity patterns are decomposed into independent components (IC's), where each component could either correspond to a



(a) Channel activities versus time



(b) ICA component activities versus time

Figure 2.1: ICA decomposition of a noisy segment of EEG (a) into independent components (b). Artifacts have not been isolated into a few components.

cortical or artifactual source. By identifying the artifactual components, setting them to zero in the component domain, and back-projecting the data to the sensor domain, it is possible to recover an artifact-free version of the data.

In practice, however, ICA might not be able to completely group the artifactual sources into a few isolated components. In order to demonstrate whether ICA can effectively remove different artifacts from our data, we have applied the infomax-ICA algorithm using the EEGLAB toolbox [65] on a raw segment of the multi-channel data in Figure 2.1. Figure 2.1a depicts 30 seconds of raw 60-channel EEG in the sensor domain, while Figure 2.1b demonstrates 60 Independent components found in this data segment. It is observed that ICA fails to separate the artifacts into a few identifiable components, as for instance, the muscle artifact seen during the 8th and 22nd second of the recording has been spread out to most of the independent components in Figure 2.1b. Also, it appears that the eye movement artifacts beginning on the 15th second have been successfully isolated into the first component. However, removing the first component does not fully eliminate the eye artifacts, suggesting that other components are also contributing to these artifacts. In such cases where many components are found to be artifactual, artifacts cannot be eliminated by nullifying their corresponding components, as setting many components to zero would amount to loss of cortical data.

We speculate the following as potential reasons as to why the ICA method fails to separate the artifactual sources successfully. First, there is a trade-off between a reliable decomposition and the signal stationarity. As suggested in [66], ICA methods require a large number of data points for reliably decomposing the data. This means that long segments of EEG are required to provide sufficient data points, while during these long segments the nature of the sources might vary significantly with time. In this sense, ICA is able to isolate the artifactual sources which remain fairly constant in time and space, and does not guarantee to separate transient artifacts occurring from time to time at random electrodes, as is the case with most of the artifacts seen in our data. Second, ICA performs best in scenarios with the same number of sources and sensors [64]. It is commonplace in EEG literature to assume the number of independent sources to be the same as the number of electrodes, while there is no justification for the validity of this assumption. In fact, EEG is the summation of many complex cortical functions and sources, and

it might not be safe to assume that the number of cortical and artifactual sources does not exceed the number of electrodes. Lastly, ICA is based on the assumption that the independent components are maximally non-Gaussian. While true distributions of the EEG sources are not known, evidence to back the fact that cortical or artifactual sources are non-Gaussian is also lacking.

Artifact Rejection by Visual Inspection

Given our observations, we have thus chosen not to use ICA for artifact rejection, and have instead rejected the artifactual channels or segments of the data by visual inspection. Approximately 5 hours of EEG recordings were visually inspected in the time domain while artifactual channels and time segments were tagged for removal using EEGLAB's interface. Electrodes with frequent saturations and those with poor skin contact, judged by their abnormal activity patterns throughout the length of the recording, were removed from the data and the analysis was based on stable channels. Time periods containing broadband muscle artifacts or any other irregular activities were also removed from the data when possible. Occurrence of eye blinks and eye movements was generally not a criterion for data rejection since their frequency content is usually below 15 *Hz* and does not overlap with the gamma band frequencies. However, these artifacts were removed in case of rarity to allow for alpha band analyses (in recordings such as those corresponding to the matching task, blinks happened very frequently and hence were not removed in order to preserve data). As for powerline interference, there was no need for application of 50 *Hz* notch filters to recordings acquired in LSBB. No 60 *Hz* notch filter was used for recordings at ICORD either, owing to the fact that the battery-operated acquisition system was also able to minimize external electromagnetic power-line interference automatically using well-calibrated differential amplifiers.

2.2.2 Pre-processing

Segmentation

After obtaining artifact-free recordings for all subjects and all tasks, we segment the long recordings corresponding to each task into consecutive non-overlapping

epochs of 10 seconds. Segmentation facilitates investigation of task-related changes in EEG and leads to more stable results, as it increases the number of samples per recording and decreases the relative non-stationarity of longer epochs. Moreover, epochs appearing as 'outliers' in the final results can easily be detected and removed as we are interested in broad spectral trends and not transient effects.

Re-referencing

EEG is a measure of voltage difference between an electrode placed at the position of interest and a reference electrode. Dependence of the recorded multi-channel data on the reference electrode causes any electrical activity on the reference electrode to be present in all other electrodes. In our data, the mid-prefrontal electrode FPZ was used as reference throughout all recordings. Since ocular artifacts usually have a topographical distribution peaking around the prefrontal channels, this choice of reference causes the ocular artifacts to spread to all other channels. Moreover, spatial proximity of an electrode to the reference electrode will cause smaller potentials to be picked from the electrode site. Hence, our choice of reference might cause relative attenuation of frontal potentials and lead to topographical biases in the end results.

To overcome problems of this sort, the data can be re-referenced to any other reference channel or combination of channels. Because re-referencing is a linear transformation of the data, it can be performed offline after the data has been recorded. We have chosen to reference the data to the average reference, which is a popular and theoretically sound choice of the new reference in high-dimensional montages. Re-referencing to the average reference is performed by subtracting from each electrode the instantaneous average across all electrodes as follows:

$$x_i^{reref}(t) = x_i(t) - \frac{1}{N} \sum_{j=1}^N x_j(t), \quad i = 1, \dots, N \quad (2.1)$$

where x_i^{reref} denotes the re-referenced version of the signal x_i at electrode i , and N is the total number of electrodes (60 in our case). From another point of view, average referencing can be regarded as spatial DC rejection of the multi-channel EEG in order to highlight and spatially sharpen the local activities over time.

2.3 Data Analysis

2.3.1 Stockwell Transform

Time-frequency transforms are essential for analyzing non-stationary signals, i.e. signals whose statistical and spectral properties change over time. Two of the most commonly used time-frequency transforms in signal analysis are Short Time Fourier Transform (STFT), and Wavelet Transform (WT).

The STFT was developed as an extension of the Fourier Transform by localizing the frequency spectrum via a sliding window with smooth edges. Generally, one has to choose between a narrow window which results in poor frequency resolution, and a wide window which results in poor time resolution. This means that STFT is not a suitable tool for analysis of signals with relatively wide bandwidths which change rapidly with time. In order to overcome this limitation, the Wavelet Transform was developed to analyze the signal with different resolutions at different frequencies. WT performs a multi-resolution analysis by decomposing the signal into a series of dilated and translated wavelets, such that high frequencies are localized into a smaller time interval than low frequencies [67].

Even though WT is an excellent tool in various applications such as denoising and finding signal irregularities, it has a number of drawbacks as well. First, the phase information of the WT is not completely understood, as it is locally defined based on the wavelet's center point and it does not maintain a fixed reference. Moreover, the non-uniform time-frequency tiling on the analyzed signal may result in biased energy representations. Specifically, the amplitude in WT is normalized in such a way that higher frequency components are more attenuated than low-frequency components [67]. These properties are undesirable in applications where intricate high-frequency components are the main attributes that are sought after in a signal.

The Stockwell Transform [53], also known as the S-Transform, is a variant of STFT and/or an extension of WT developed in an attempt to overcome these issues. The S-transform of the signal $x(t)$ is given by

$$S(\tau, f) = \int_{-\infty}^{+\infty} x(t) \frac{|f|}{2\pi} e^{-\frac{(\tau-t)^2 f^2}{2}} e^{-i2\pi f t} dt \quad (2.2)$$

The above formulation can be viewed as the STFT of $x(t)$ windowed by a localizing Gaussian function $g(t) = \frac{1}{\sqrt{2\pi}\sigma} e^{-\frac{(t-\tau)^2}{2\sigma^2}}$, where the width of the Gaussian window $\sigma = \frac{1}{|f|}$ is inversely proportional to frequency [67].

From the point of view of WT, Eq. (2.2) can also be seen as a 'corrected' version of the continuous wavelet transform of $x(t)$ using a complex Morlet wavelet given by $\phi(t) = \frac{1}{2\pi} e^{-\frac{t^2}{2}} e^{2\pi i t}$:

$$\begin{aligned} W(\tau, a) &= \int_{-\infty}^{+\infty} x(t) \frac{1}{\sqrt{|a|}} \phi^*\left(\frac{t-\tau}{a}\right) dt \\ &= \int_{-\infty}^{+\infty} x(t) \frac{1}{\sqrt{|a|}} \frac{1}{2\pi} e^{-\frac{(t-\tau)^2}{2a^2}} e^{-2\pi i \left(\frac{t-\tau}{a}\right)} \\ &= \sqrt{|a|} \int_{-\infty}^{+\infty} x(t) \frac{1}{2\pi|a|} e^{-\frac{(t-\tau)^2}{2a^2}} e^{-2\pi i \frac{t}{a}} e^{2\pi i \frac{\tau}{a}} dt. \end{aligned} \quad (2.3)$$

Where $*$ denotes complex conjugation. Letting $a = \frac{1}{|f|}$ yields

$$W(\tau, f) = \frac{1}{\sqrt{|f|}} e^{2\pi i f \tau} S(\tau, f), \quad (2.4)$$

Or equivalently,

$$S(\tau, f) = \sqrt{|f|} e^{-2\pi i f \tau} W(\tau, f). \quad (2.5)$$

Hence, the S-Transform is a generalization of the complex Morlet wavelet transform with the following modifications: 1) The multiplicative amplitude term $\sqrt{|f|}$ causes the localizing Gaussian window to always have unit area, thus providing a frequency-invariant amplitude response; and 2) the phase correction term $e^{-2\pi i f \tau}$ which remains stationary while the Gaussian window is translated, enables the S-Transform to maintain absolute phase information relative to time $\tau = 0$. Therefore, the S-Transform inherits the advantages of STFT and WT at the same time, and it is in regard to these favorable properties that we choose it for analysis of high-frequency EEG.

Given a segment of single-channel EEG, we can thus measure activity within any frequency band and time window using the S-Transform in much the same way as STFT. We will compute the total energy in the frequency band of interest

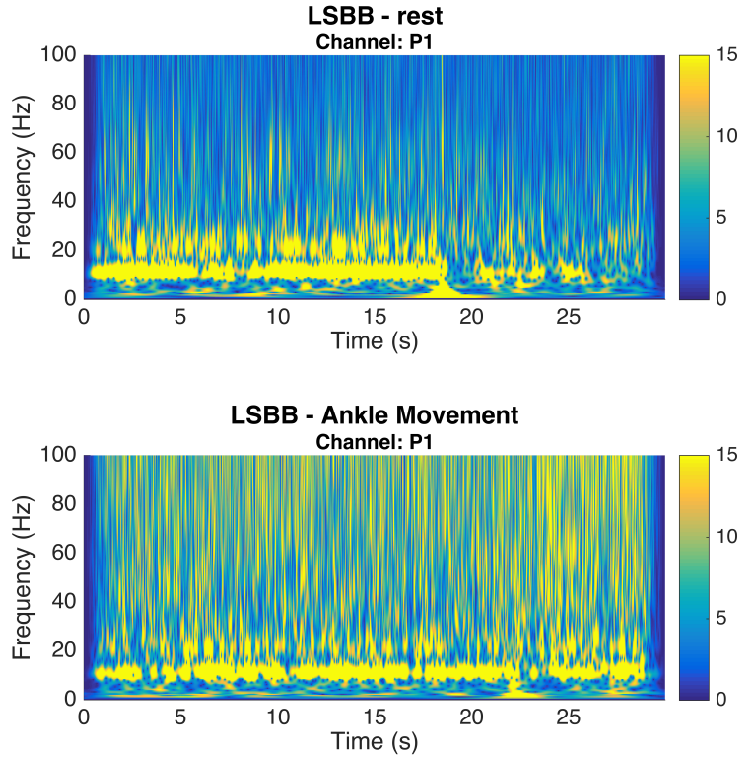


Figure 2.2: Stockwell transform magnitude of resting state (top) as well as that of a motor task (bottom) from a single channel, single subject, and single environment (LSBB). The motor task has suppressed the low-frequency activity and has caused increases in gamma band energy throughout the continuous recording.

by integrating the S-transformed signal in the time-frequency space:

$$E_{[f_L-f_H]} = \int_{f_L}^{f_H} \int_{t_i}^{t_f} |S(t, f)|^2 dt df \quad (2.6)$$

where $E_{[f_L-f_H]}$ refers to the total energy of the S-Transform summed over frequencies f_L to f_H and times t_i to t_f . Figure 2.2 depicts the S-transform magnitude of raw EEG signals of one subject during 30-second intervals of rest and a repetitive motor activity (ankle movement) in the low-noise recording environment (LSBB) and a single parietal channel (P1). Comparing the figure on top (resting state) with the one on the bottom (motor task), we immediately observe that the motor

activity has caused power increases within the gamma band ($f > 30 \text{ Hz}$). More specifically, computing E_α , E_β , and E_γ , leads to the observation that the total S-Transform energy in alpha, beta, and gamma band has changed from 7.8, 4.3, and 2.6, to 5.6, 3.9, and 9.3, from the resting state to the motor condition, respectively. We can therefore conclude that for this specific EEG segment, subject, channel, and environment, the motor task has caused decreases in alpha and beta band and an increase in gamma band spontaneous activities.

2.3.2 Comparison of the Two Environments

One of the main goals of conducting this study was to further assess the quality of signals acquired in the low-noise environment by way of comparison with those acquired in a typical noisy environment. In particular, the objective is to search for task-specific changes in EEG, exhibited as power increases within the gamma band, and see if they are more prominent and better reflected in LSBB signals due to higher signal to noise ratio. For this section, we will use data from four subjects who are common to both environments in order to have an unbiased comparison of the two environments.

Figure 2.3 depicts the same information shown in Figure 2.2, with similar recordings (same subject, channel, and conditions) from the hospital environment included for comparison. We observe that even though the motor activity has caused gamma band power increases in both environments, this increase is more prominent in LSBB than in ICORD.

To quantitatively assess the task-specific changes in the gamma band EEG across subjects, channels, and conditions, we calculate the task-rest gamma band energy ratios of the S-transform and compare them between LSBB and the hospital environment.

We measure the high frequency activity during each of the epochs by computing the total gamma band energy of the epoch in the time-frequency space, defined in Equation (2.6) and with f_L , f_H , t_i , and t_f values set to 30 Hz, 100 Hz, 0 s, and 10 s, respectively. Consequently, responses to each task for each subject are expressed as task-rest ratios; that is, given there are N epochs corresponding to the rest condition and M epochs belonging to a particular task, we compute a total of

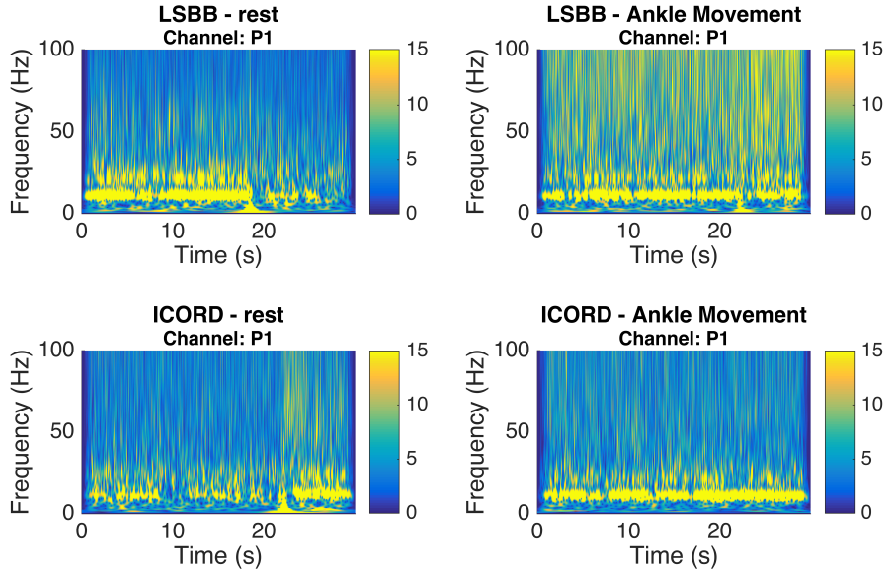


Figure 2.3: Stockwell transform magnitude of resting state (left) as well as that of a motor task (right) from a single channel and a single subject, at both LSBB (top) and ICORD (bottom). The task-specific increase in gamma band energy is more prominent in LSBB.

$M \times N$ ratios by dividing the total gamma band energy of each task epoch by the total gamma band energy of each of the resting-state epochs.

This process is done in a channel-wise manner, resulting in MN task-rest ratio values for each channel. Since the high-dimensional results are difficult to interpret among subjects and conditions, some data reduction across channels is necessary. In order to present the results in a more compact manner, we classify the electrodes into nine functionally different brain regions (see Table 2.1 and Figure 2.4). For each task, we can then compare the entire set of ratios (including all four subjects common to both environments) in LSBB with that of the hospital environment at each of these brain sites.

The results from time-frequency analysis across epochs of all subjects in both environments are summarized in Figure 2.5. These plots allow for comparison of the distribution of gamma band task-rest ratios in LSBB and ICORD across different brain regions.

Brain Region	Electrodes
Prefrontal	FPZ, FP1, FP2, AFZ, AF3, AF4, AF7, AF8
Frontal	FZ, F1, F2, F3, F4, F5, F6, F7, F8, FCZ, FC1, FC2, FC3, FC4
Central	CZ, C1, C2, C3, C4, CPZ, CP1, CP2, CP3, CP4
Left Temporal	FC5, FT7, C5, T7, CP5, TP7
Right Temporal	FC6, FT8, C6, T8, CP6, TP8
Left Parietal	P3, P5, P7, PO3, PO7
Right Parietal	P4, P6, P8, PO4, PO8
Parietal	PZ, P1, P2, POZ
Occipital	OZ, O1, O2

Table 2.1: Grouping of the electrodes in a 10-10 montage based on their locations

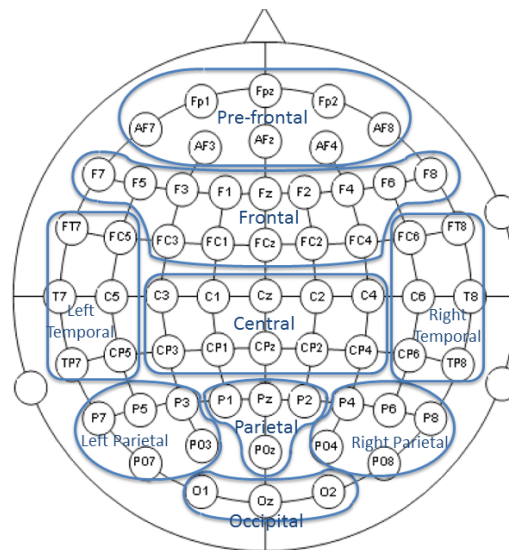
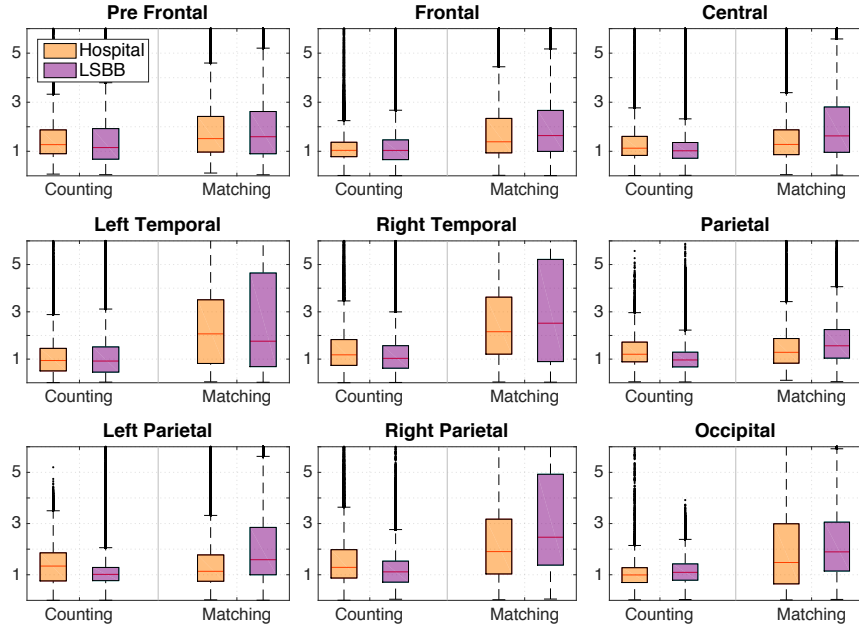
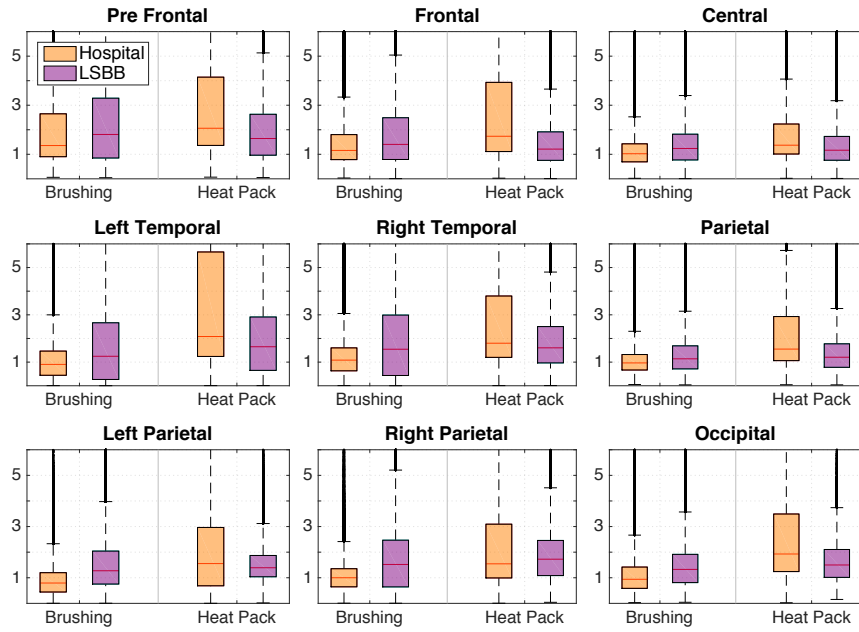


Figure 2.4: Topographical map of electrode groups based on the classification in Table 2.1

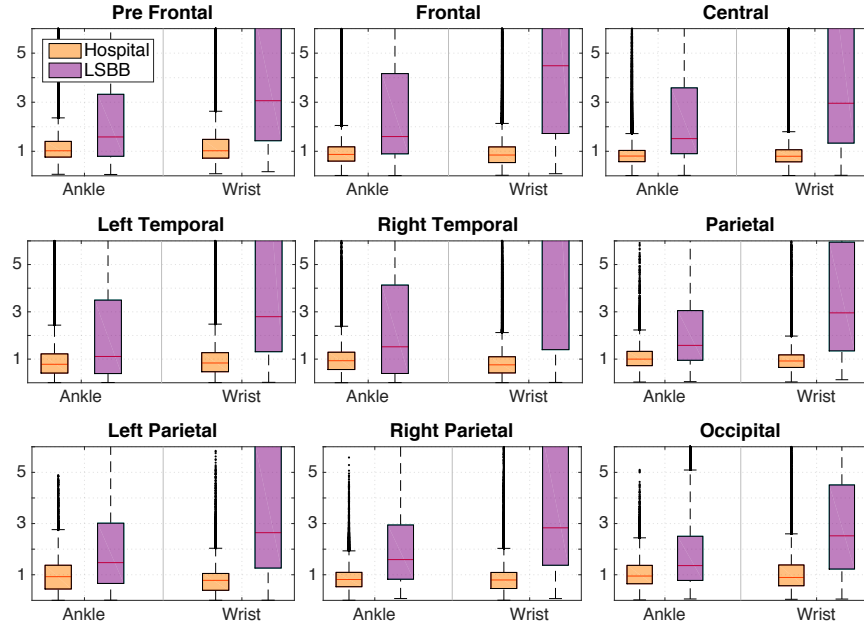
A quick look at Figure 2.5c reveals that for both of the motor tasks, the gamma band motor-rest ratios are significantly larger and more readily detected in LSBB across all regions of the brain. While the median of motor-rest ratios at LSBB is always greater than one, the median of ratios at the hospital stays close to one, suggesting that the gamma band activity in motor tasks was not readily detectable



(a) Cognitive Tasks



(b) Sensory Tasks



(c) Motor Tasks

Figure 2.5: Box plots demonstrating the distribution of task-rest gamma band energy ratios across different subjects in different brain regions, conditions, and environments. Subplots of each sub-figure correspond to the nine groups of electrodes (brain regions) according to Table 2.1. We have grouped the tasks into three categories: cognitive tasks (Fig. 3a) including counting and matching, motor tasks (Fig. 3b) including right ankle movement and right wrist movement, and right hand sensory tasks (Fig. 3c) including brushing and application of a heat pack. Tasks belonging to each category are shown alongside each other. For each task, we have shown a boxplot of the task-rest ratios acquired in the hospital environment (left) along with a boxplot of the ratios acquired at LSBB. Shown in the plots are the median value, as well as the 25% and 75% quartiles, and the whiskers representing $\pm 2.7\sigma$ or 99.3 percent coverage given the data is normally distributed.

at the hospital. Interestingly, LSBB ratios are consistently higher during the wrist movement task compared to the ankle movement task, while no significant difference between wrist and ankle movement is observable at ICORD.

We have depicted the ratios for cognitive tasks in Figure 2.5a. Although having slightly higher values in ICORD, backward counting-rest ratios are mainly distributed around one in both environments, suggesting that spontaneous gamma band activity may not correlate with continuous counting tasks. This was also found to be the case in a previous study [52]. On the other hand, the median of matching-rest ratios is mainly greater than one in both environments, and is higher in LSBB at all brain regions except for the left temporal region. As an explanation for why a global increase in ratios is not seen at LSBB, it could be claimed that the increase in gamma band due to matching is more focused, contrary to the motor functions which exhibit a more global cortical response. Thus, in brain regions where the gamma-band content is boosted due to the cognitive activity associated with the matching task, the ratio increase is more prominent within the low-noise settings at LSBB than in the hospital environment.

Brushing-rest and noxious heat-rest ratios were also compared between the two environments in Figure 2.5b. This figure demonstrates that the median of brushing-rest ratios is slightly higher in LSBB compared to the hospital, thus revealing the potential of LSBB in identifying the brushing-induced high frequency activity. However, the heat-rest ratios are generally lower in LSBB than in the hospital environment. Explaining this issue, it is worth mentioning that the average of the VAS pain ratings across all recordings and all subjects was 5.5 at the hospital and 1.5 at LSBB, suggesting that despite the efforts to keep the experiment conditions equal, the subjects reportedly experienced more pain in the hospital facility than in LSBB. We might therefore hypothesize that the lower ratios in LSBB are caused by the lower pain experience in comparison with ICORD, which would in turn yield lower gamma band activity in LSBB as the strength of gamma band oscillations has been shown to correlate well with the intensity of the perceived pain [17].

Overall, our results demonstrate that functionally correlated gamma-band EEG patterns can be better detected in low-noise conditions when compared with a typical hospital environment. This motivates the design of more informative studies with the end goal of defining potentially novel and predictive high-frequency EEG (gamma-band benchmarks) for a better understanding of central neuronal function and CNS disorders.

2.3.3 Task-specific EEG Changes in Both Environments

The analysis in section 2.3.2 was based on subjects common to both environments in order to have a fair comparison groundwork. However, another objective of this thesis is to search for task-specific EEG correlates among all subjects, regardless of the recording environment. In this section, we will examine the spontaneous power changes in EEG using data from all subjects and all environments. Moreover, we will also investigate other frequency bands in addition to gamma band. Our goal is to present a comprehensive analysis on the topographical and frequency-specific changes in EEG between different conditions to observe the effect of each task on brain's rhythmic activity.

We adopt two different approaches to analyze the effects of two variables in question: frequency and topology. The role of different frequency bands is quantitatively assessed via Power Change Ratio (PCR), a measure nearly identical to S-Transform task-rest ratio introduced in the previous section. On the other hand, topographical analysis of different frequency bands is performed by strict statistical significance testing to minimize spurious false-positive results in examination of spatial patterns of EEG.

- **Power Change Ratio**

We define Power Change Ratio (PCR) from the i -th resting-state epoch R_i to the j -th task epoch T_j in each frequency band B as

$$PCR_{i,j} = \frac{E_{T_j}^B - E_{R_i}^B}{E_{R_i}^B} \quad (2.7)$$

where $E_{(\cdot)}^B$ denotes the total epoch energy in the time-frequency space as elaborated in equation (2.6); and i and j range from 1 to the total number of rest and task epochs, respectively. Contrary to task-rest ratios, task-specific increase and/ or reduction in energy cause the PCR to elicit positive and negative values, respectively, hence yielding a more intuitive measure of energy changes.

In what follows, we use the PCR values to depict relative task-rest power changes at each region of the brain. Taking a similar approach as the previ-

ous section, we first compute MN channel-wise PCR values from all combinations of N resting-state epochs and M epochs belonging to a particular task. We then group these values according to the regioning scheme discussed in section 2.3.2. Lastly, we examine the mean and standard deviation of all PCR values in a particular brain region across subjects, electrodes, and epochs, using all recordings from all eight subjects. This procedure is repeated for different frequency bands; namely, alpha, beta, and our so-called 'low gamma' and 'high gamma' sub-bands detailed in Table 2.2.

Name of Frequency Band	Lower And Upper Frequency Bounds (Hz)
Alpha	[7 – 12]
Beta	[12 – 30]
Low Gamma	[30 – 65]
High Gamma	[65 – 100]

Table 2.2: Different frequency bands used in our analysis. Low Gamma and High Gamma bands are custom-defined ranges to allow for a more refined analysis of the gamma band.

- **Statistical Significance Testing**

Furthermore, in order to accurately infer the topographical distribution of task-specific energy increases using all epochs at hand, we introduce 'significance maps': For each channel, the S-Transform energy of all task epochs is statistically compared to energies of all rest epochs to test if the median of energies in the task condition is greater than that of the resting-state condition. Since channel-wise energy values are not normally-distributed, we use the nonparametric Wilcoxon rank sum test to assess statistical significance between the two conditions. This procedure yields a binary map $M_{60 \times 1}$ for each subject in which $M(i) = 1$ indicates statistically significant energy increase at channel i . The significance maps for different subjects are then averaged to yield an average map of topographical S-Transform energy increases in the desired frequency band. Finally, the resulting average significance map $\bar{M}_{60 \times 1}$ is arranged in topographical plots using spatial information from all electrodes, where 'brighter' spots represent local significant task-specific en-

ergy increases which have survived subject averaging. The algorithms used in generating these plots typically utilize quadratic interpolation between the nearest electrodes to allow for smooth, more realistic transitions between the values of different electrodes, and hence aid in visual interpretation of the results.

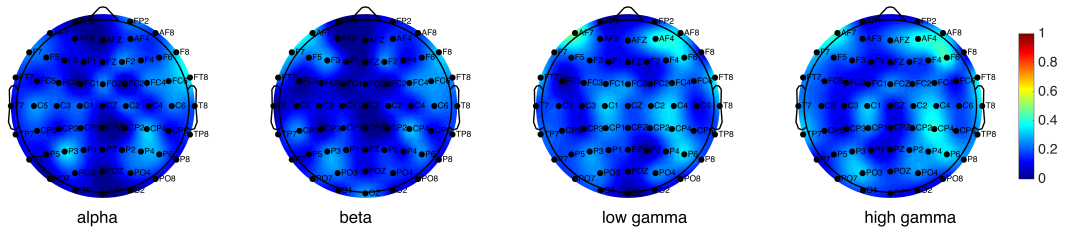
In the following, we present the results of applying above analysis methods on each of the tasks using the aggregate data from all subjects in ICORD and LSBB. We will categorize our results based on each of the cognitive, sensory, and motor tasks.

Cognitive Tasks

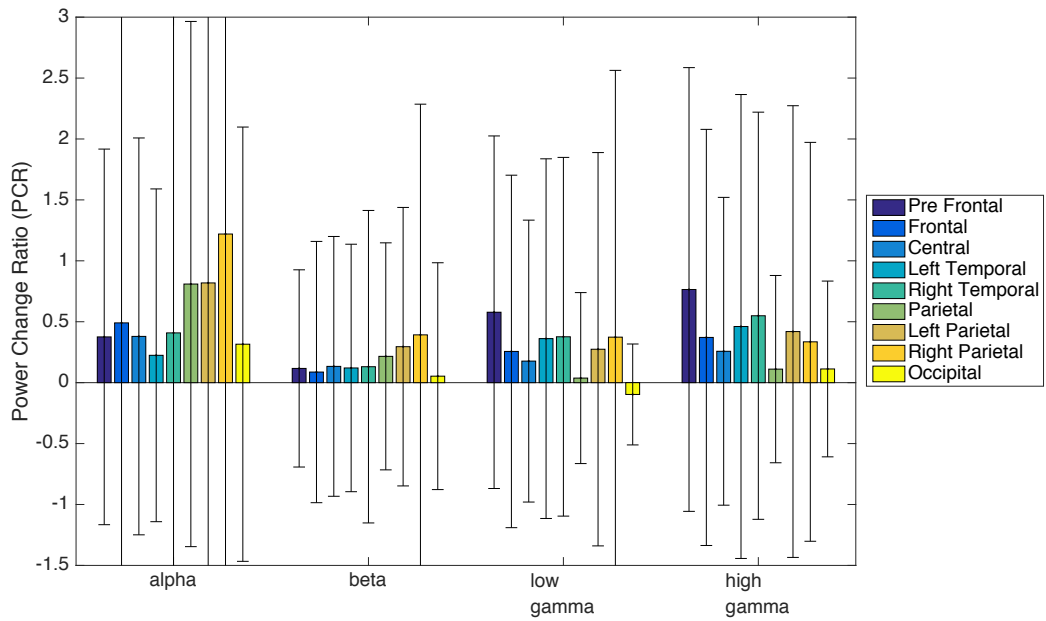
Figure 2.6a depicts significance maps of the backward counting task in alpha, beta, low gamma, and high gamma frequency bands. It is evident from the topographical plots that during the counting task, spontaneous alpha and beta activity are localized more or less symmetrically on the parietal lobes, while prefrontal lobes as well as centro-parietal electrodes show more activation in the gamma band.

Moreover, Figure 2.6b illustrates the quantitative PCR information for each brain region and frequency band, where the colored bars represent the average PCR values among all subjects and all electrodes in a specific brain region, and the error bars represent the standard deviations of the aforementioned PCR values. We observe that on average, spontaneous alpha band has the highest increase in energy during counting. We believe that this was a side-effect of keeping the subjects' eyes closed during counting, and not a direct influence of the cognitive task, since these large power increases in the alpha band have not passed the significance test while being compared with resting-state energies in Figure 2.6a.

Alpha and beta band patterns depicted in Figure 2.7 for the matching task are observed to be more centralized and concentrated on the right parietal region. Similarly to Figure 2.5a, the matching task has caused more activity within the gamma band than the counting task. Interestingly, mid-parietal and occipital areas have reduced energies during matching in alpha and beta bands, while a global increase in gamma band energies (less so in central areas) is observed, and more areas of the brain are involved in cognitive processing in high gamma ranges compared to

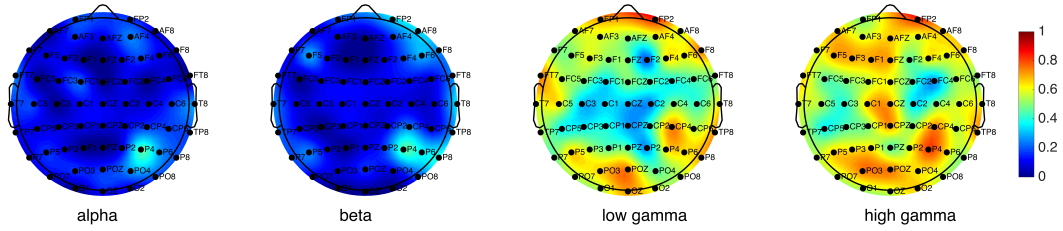


(a)

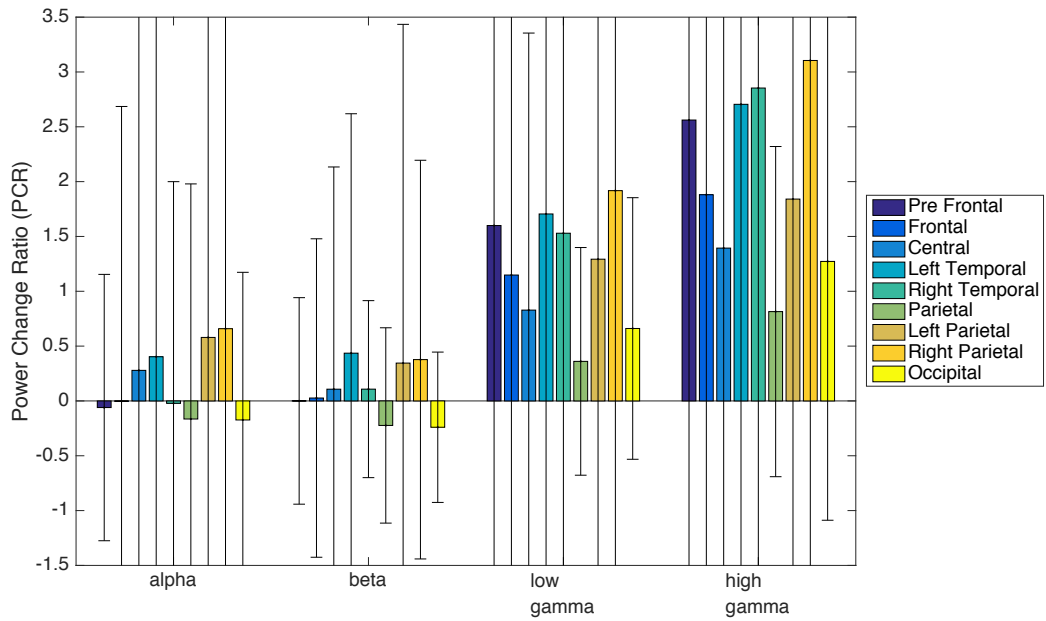


(b)

Figure 2.6: **a)** Significance maps obtained from channel-wise statistical testing between the rest condition and backward counting task at four frequency bands; **b)** Power Change Ratios of the backward counting task at different frequency bands and different brain sites.



(a)



(b)

Figure 2.7: **a)** Significance maps obtained from channel-wise statistical testing between the rest condition and the matching task at four frequency bands; **b)** Power Change Ratios of the matching task at different frequency bands and different brain sites.

the lower gamma rhythms.

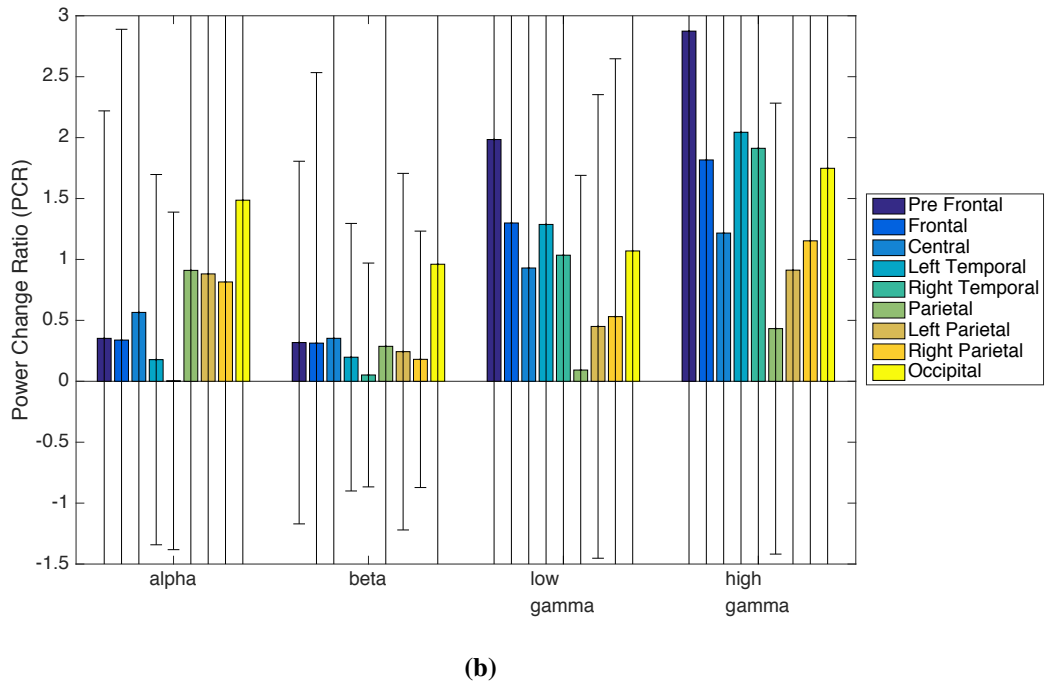
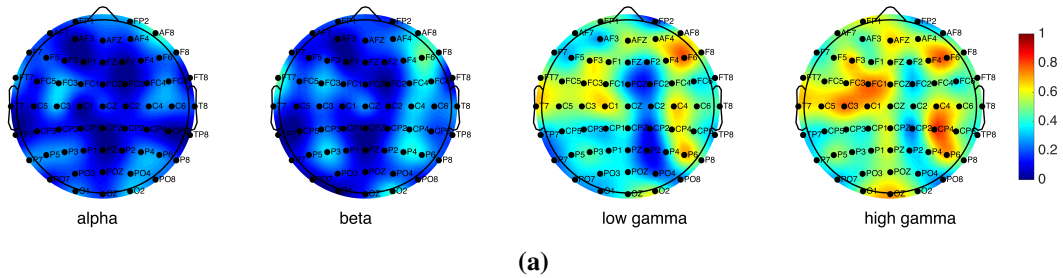
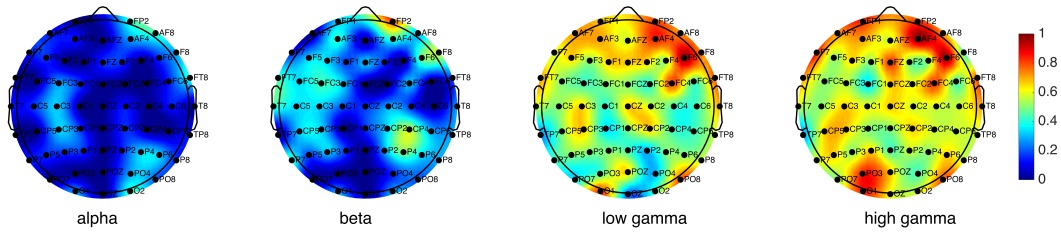


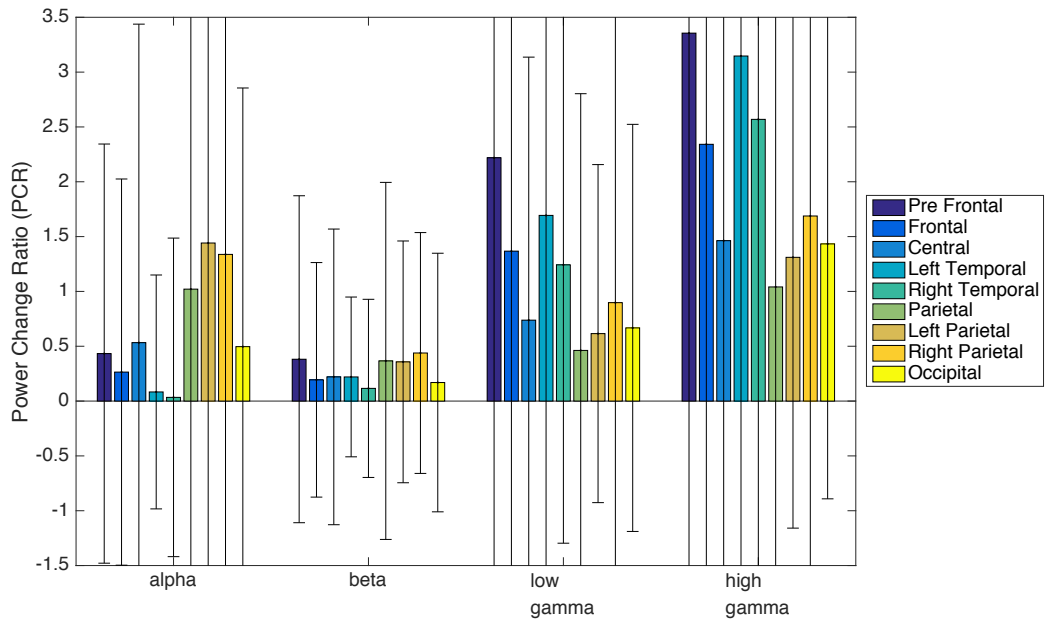
Figure 2.8: **a)** Significance maps obtained from channel-wise statistical testing between the rest condition and the brushing task at four frequency bands; **b)** Power Change Ratios of the brushing task at different frequency bands and different brain sites.

Sensory Tasks

According to Figure 2.8, brushing of the right hand causes alpha, beta, and gamma energy increases in the contralateral (left) central electrodes. With increasing fre-



(a)

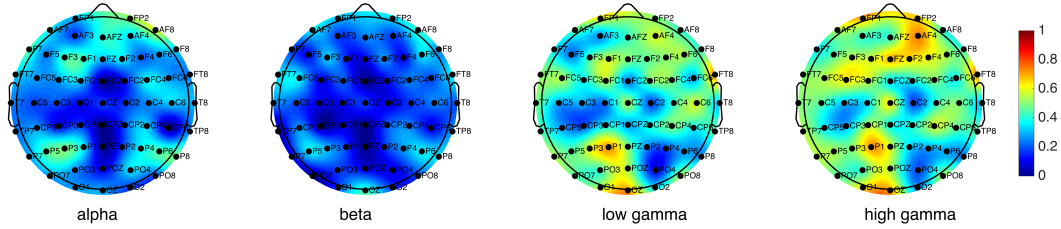


(b)

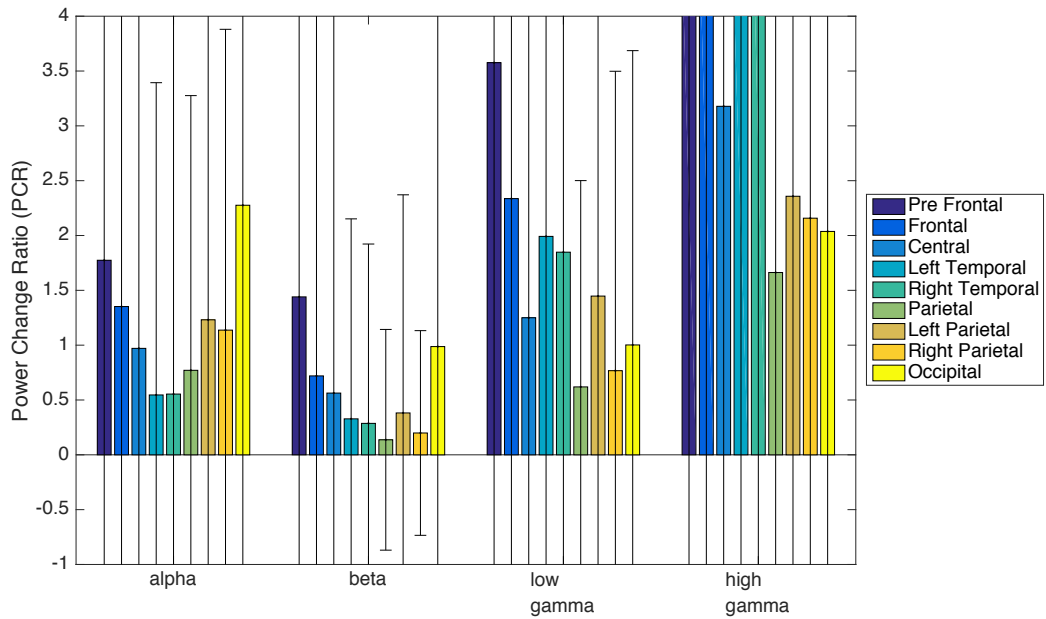
Figure 2.9: a) Significance maps obtained from channel-wise statistical testing between the rest condition and application of hot packs at four frequency bands; b) Power Change Ratios during the application of hot packs at different frequency bands and different brain sites.

quency, centro-parietal lobes on the ipsilateral region (channels C4, CP4 and P6) also take part in information processing. On the other hand, Figure 2.9 demonstrates that holding hot packs has caused energy increases within the contralateral central region, most notably in the beta band, as well as significant prefrontal gamma band activity (Figure 2.9).

Motor Tasks



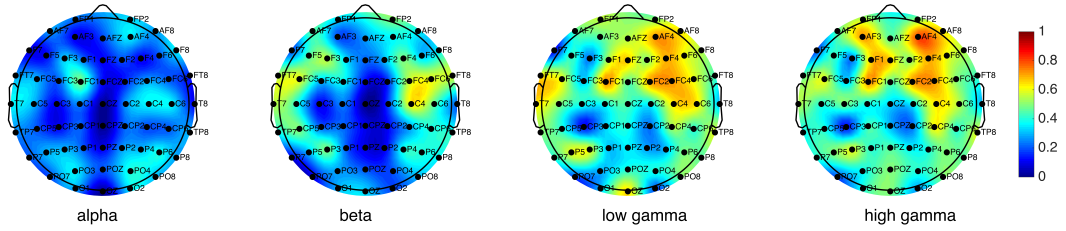
(a)



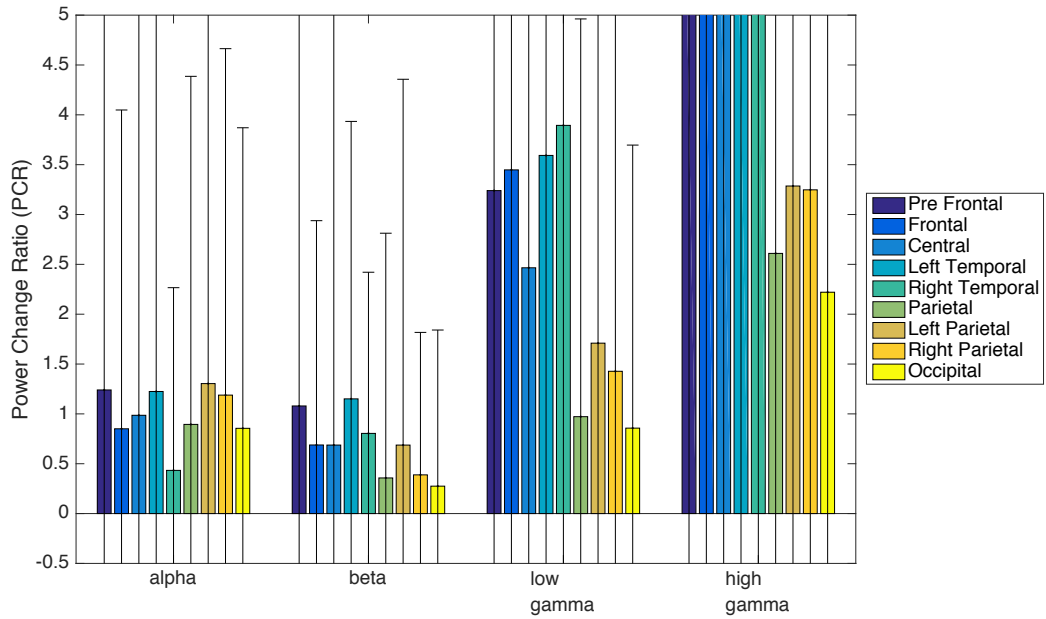
(b)

Figure 2.10: a) Significance maps obtained from channel-wise statistical testing between the rest condition and the ankle movement task at four frequency bands; b) Power Change Ratios of the ankle movement task at different frequency bands and different brain sites.

Figure 2.10 illustrates the effect of ankle movement on EEG at different frequency bands. Most notable effects are alpha and gamma prefrontal energy enhancements, symmetrical alpha and beta energy increases within temporal regions, and gamma energy enhancements on the contralateral P1 electrode. While beta



(a)



(b)

Figure 2.11: **a)** Significance maps obtained from channel-wise statistical testing between the rest condition and the wrist movement task at four frequency bands; **b)** Power Change Ratios of the wrist movement task at different frequency bands and different brain sites.

band is minimally contributing to the energy increases during ankle movements, it is more active during wrist movements as seen in Figure 2.11. Moreover, gamma band activity seems to be more focused on the frontal areas during movements of the wrist in comparison with the ankle movement task.

2.4 Discussion And Conclusions

In this chapter, we used the Stockwell Transform to analyze spectral and spatial aspects of 60-channel EEG recordings corresponding to different cognitive and sensorimotor conditions.

We first compared the gamma band (30 – 100 Hz) content of signals acquired at the low-noise environment with those collected at the hospital facility in section 2.3.2, and found significant differences between the two environments in their ability to detect task-specific spontaneous gamma band oscillations, especially during motor tasks. In other words, we observed higher task-rest spontaneous gamma band energy ratios at LSBB in comparison with ICORD. This is clearly an advantage for studies in a low-noise environment such as LSBB, indicating its potential for detection of EEG benchmarks related to understanding central nervous system (CNS) control of basic motor tasks or early detection of disorders associated with changes in motor behaviors (e.g. Epilepsy, Parkinsons disease, etc.). Low-noise environments, like the LSBB, would also facilitate a greater understanding for potential subtle changes in cortical plasticity after CNS motor injuries (e.g. spinal cord or brain damage).

In section 2.3.3 of this chapter, we used data from all subjects, including those who were not common to both environments, and carried out the same Stockwell transform time-frequency analysis method; though with slightly different approaches to highlight functional differences of various frequency bands and different brain sites. Contrary to section 2.3.2 where the analysis was only based on the gamma band, in this section we also examined the role of alpha and beta bands, as well as separated the upper and lower halves of the gamma frequency range into two subbands. Each of the tasks and conditions in our study protocol integrate unique and complex spectral and spatial EEG patterns. Since a detailed neurological analysis of each of the task-specific EEG patterns is beyond the scope of this

thesis, we have presented a brief summary of the observed patterns for each task in section 2.3.3, and we will leave further analyses to future publications. We will, however, state one unifying observation among all of the tasks: high-frequency EEG activity is not as centralized and localized to specialized brain areas as lower-frequency activity; rather, it seems that the brain tends to employ more and more large-scale neuronal networks with high-frequency synchronization in higher-level stages of cognitive and sensorimotor information processing.

This work bore a number of limitations. First, the number of subjects and hence the size of our dataset was not large enough to yield statistically rigorous results. In fact, the large standard deviations seen in figures in section 2.3.3 as long error bars is in part due to the high between-subject variability observed in the results. Moreover, the data at LSBB was improperly annotated. In other words, the data during each task was mixed with resting-state epochs, and the only markings on the dataset were put on rough start and end points of different tasks, not the resting-state epochs in between them (see Appendix A). This could have introduced biases and imperfections in our data analysis pipeline. It also limits our scope of analysis of the data; for instance, since the correspondence between the VAS ratings for the heat sensory task and actual time points in the dataset was unclear, the VAS ratings could not be used to correlate the strength of gamma band oscillations with subjective pain experience. (the limitations of the study protocol are revisited in detail in section 4.2).

To address the limitations of the current work, studies using a larger number of subjects are necessary for more stringent statistical validation and more confident conclusions. One might also consider designing a protocol for detection of evoked and induced potentials with time-locked experimental trials as opposed to spontaneous EEG. Interactive automated acquisition systems, such as those using computer-generated auditory or visual cues for start and end points of performing tasks would greatly enhance the capabilities of our future analyses.

Chapter 3

Granger-Causal Connectivity Analysis

3.1 Introduction

3.1.1 Motivation for Connectivity Analysis

With the dawn of the 21st century, the neuroscience community has emphasized the need to move beyond *functional segregation*, which refers to the existence of specialized neuronal populations to form functionally segregated cortical areas, to studies of *functional integration* of the brain; i.e. viewing the brain as an interconnected system in which the interplay among different parts acts as a crucial element in neural operation and formation of coherent cognitive and behavioral states [68]. Historically, this notion of 'brain connectivity' might have stemmed from Cajal's neuron doctrine [69], stating that while the neuron is a separable entity in itself, its operation largely depends on the input gathered from other neurons. Over the years, these ideas have resulted in a large number of multidisciplinary tools and methodologies for studying the large-scale interactions between different, possibly remote brain regions and unveiling the so-called human *Connectome*.

Brain connectivity patterns are dynamic in nature; links among neuronal assemblies may form or disappear in milliseconds [70], allowing for fast and tran-

sient information transfer among brain regions. Therefore, it is important to study connectivity in a framework that encompasses both time and space simultaneously. While the popular fMRI modality allows for high spatial resolution in studying brain function, efforts in fMRI are generally complicated by its relatively low temporal resolution. Moreover, recent research suggests that typical assumptions and statistical methods used in fMRI introduce a high number of false positives and lead to erroneous conclusions [71]. On the other hand, the low-cost, non-invasive scalp EEG offers substantially higher temporal and spectral resolution. With the aid of proper computational data analysis tools and an acquisition system comprising of densely distributed electrodes, EEG is an attractive candidate for studying rapidly changing spatiotemporal interactions among brain regions.

3.1.2 Different Categories of Connectivity

Connectivity patterns of the brain can be studied from several perspectives. Generally, studies of connectivity fall into one or more of three categories: anatomical, functional, and effective connectivity.

Anatomical or *structural* connectivity aims at describing the biophysical (i.e. axonal) communication links between neuronal assemblies. One example of the methodologies in this field is the neuroanatomical tract tracing [72], an invasive technique to provide information about direct axonal connections *in vivo*. Anatomical connectivity can also be studied non-invasively, though with lower spatial resolution, by means of diffusion weighted imaging techniques such as diffusion tensor MRI (DTI) [73].

The goal of *functional* connectivity, on the other hand, is not to understand the physical capability of axonal links. Rather, functional connectivity is concerned with finding evidences of statistical dependence among large-scale neuronal units, regardless of the presence of direct anatomical connections. The dependence among brain regions is typically examined by means of cross-correlation, spectral coherence, or mutual information, and therefore has no notion of direction or causation. Primary tools for the analysis of functional connectivity, including fMRI and Positron Emission Tomography (PET), have shown that functional connectivity is related to behavior in a variety of different tasks [74].

In addition to functional connectivity, *effective* connectivity attempts to understand causation among neural units, i.e. the influence that one neural system has over another. In other words, in comparison with functional connectivity, effective connectivity provides additional information about the *direction* of interactions as well as their presence. Current techniques for determining effective connectivity include Granger-causal modeling, dynamic causal modeling, structural equation modeling, and transfer entropy, applied to neuroimaging data such as fMRI as well as EEG/MEG time series [75]. Methodologies implemented in this chapter typically fall under the category of task-relevant effective connectivity. It is worth mentioning that there is not always a sharp distinction between the terminology of effective and functional connectivity, as sometimes directed connectivity relevant to a particular function might be called functional connectivity.

3.1.3 Modeling And Estimation of Connectivity

Various methods have been devised for quantification of connectivity patterns over the past decades. While most of these methods rely completely on the data to infer connectivity patterns (data-driven approaches), there are also techniques which assert specific prior assumptions on the connectivity structure (model-based approaches). Dynamic causal modeling (DCM) [49] is a popular example of a model-based technique which relies on comparing different models of connectivity based on the relative evidence for one model compared to another [50]. Structural Equation Modeling (SEM) is another hypothesis-driven approach based on explaining the observed covariance among several variables by a defined anatomical network [76]. On the other hand, correlation-based methods and information-theoretic techniques such as transfer entropy [77] and mutual information [78] exemplify methods that do not depend on prior assumptions on the model and try to find connectivity structure solely based on the data. The model-based methods are valuable when there is some validated pre-existing knowledge about the underlying dynamics of connectivity, which is usually not the case in the current state of neuroscience with so many unknown patterns of interactions that are yet to be discovered.

From a different perspective, the connectivity estimation metrics can be classified into either linear or nonlinear measures. Typically, most of the methods in the

literature are based on linear assumptions; while information-theoretic approaches or methods such as the imaginary part of coherency [79], do not assume linear relations among variables. Linear methods are generally easy to implement and are sufficient for detection of interactions such as coupling of oscillations at similar frequencies, while nonlinear methods are useful if we are interested in nonlinear forms of coupling, such as cross-frequency coupling at two different frequencies [80]. Moreover, while it may seem counter-intuitive to apply linear methods to problems of highly nonlinear nature such as EEG, it has been shown that many biomedical signals can be sufficiently characterized and analyzed by means of linear methods [81].

Connectivity metrics may also be classified into bivariate or multivariate measures. Bivariate measures find patterns of interaction among a multiplicity of signals by calculating pair-wise connectivity separately for each channel pair. On the other hand, for computing multivariate measures all channels are taken into account at once by fitting a full multivariate model. Most of the nonlinear connectivity measures such as mutual information and phase synchronization are bivariate [48]. It is shown that in the case of densely inter-connected networks, multivariate measures are strongly preferred since bivariate measures may lead to misleading and spurious connectivity patterns [48].

Through the rest of this thesis, we focus on a model-based, linear, and multivariate method based on Granger causality [82]. Originated from the field of economic time series, Granger causality describes a framework for quantifying the influence of signal $A(t)$ on another signal $B(t)$ by the ability of A to predict subsequent instances of B . Due to their simplicity, interpretability, and the minimal prior assumptions posed on the data, Granger-causal methods have been extensively used in biomedical data analysis [83]; and their use has been extended to more than two signals by means of MultiVariate AutoRegressive (MVAR) modeling [84]. Moreover, many of these methods operate in the frequency domain and have proper adaptive variants to deal with nonstationarity of the multivariate signals, thus being good candidates for analysis of connectivity within specific frequency bands of a nonstationary multivariate process such as EEG.

Until recently, analysis of connectivity was based on the implicit assumption that the pattern of interactions among brain regions remains fairly constant over the

course of performing a task or the period of data collection [74]. This assumption has led to an extensive number of studies contributing to our understanding of large-scale interactions. However, results of these studies typically represent the aggregate or average connectivity patterns 'smeared' across time. In cases such as studying the formation and propagation of epileptic seizures, however, analysis of changes in dynamic connectivity over smaller, near instantaneous time scales will lead to greater insights into the fundamentals of brain networks [85]. In this thesis, we have analyzed our data both from a static and dynamic perspective, with the results of the former and latter approaches presented in sections 3.4.1 and 3.4.2, respectively.

This chapter is organized as follows. In section 3.2 we describe the theory behind MVAR modeling and Granger-causal methods and introduce a number of connectivity measures based on Granger causality. Section 3.3 discusses the practical issues faced when these theories are to be implemented on real EEG data, as well as our methods and approaches in solving these issues. Once the theory and methods are introduced, the results of applying the static measures on our data are presented in section 3.4.1. In section 3.4.2, we extend our use of these measures to the time-varying case in order to incorporate time evolutions of the connectivity patterns.

3.2 Theory

3.2.1 Granger Causality

Granger's original definition of causality [82] is based on the fact that causes precede their effects in time, and that knowledge of the cause aids in predicting the effect. Specifically, let us assume that we are interested in predicting the value of a time series x_1 at time t based on a linear combination of its p previous values:

$$x_1(t) = \sum_{i=1}^p A_{11}(i)x_1(t-i) + \varepsilon(t) \quad (3.1)$$

where $\varepsilon(t)$ is the prediction error. If, in predicting the current value of $x_1(t)$, we incorporate also q previous values of another signal $x_2(t)$, we will attain a different

prediction error $\varepsilon'(t)$:

$$x_1(t) = \sum_{i=1}^p A'_{11}(i)x_1(t-i) + \sum_{j=0}^{q-1} A_{12}(j)x_2(t-j) + \varepsilon'(t) \quad (3.2)$$

In this context, x_2 is said to Granger-cause x_1 if it can be shown that ε' is an improvement over ε . This improvement in the prediction error needs to be assessed in a statistical sense, e.g. by performing an F-test on the variances of $\varepsilon(t)$ and $\varepsilon'(t)$, given assumptions of covariance stationarity on $x_1(t)$ and $x_2(t)$.

3.2.2 MultiVariate AutoRegressive (MVAR) Models

Granger-causal relations between signals $x_1(t)$ and $x_2(t)$ in equation 3.2 can also be inferred through parameters $A'_{11}(i)$, $i = 1, \dots, p$ and $A_{12}(j)$, $j = 0, \dots, q - 1$. These parameters, along with a similar set of parameters relating $x_2(t)$ with past values of itself and $x_1(t)$, comprise an autoregressive (AR) model. Autoregressive modeling is a simple yet effective approach for characterization of time series and their spectra. The order of the model (p , q , etc.) is the number of preceding observations included in the model and depends on the dynamics of the signal. The coefficients A_{ij} are essentially features carrying information about the behavior of the time series. In the context of Granger causality, these features represent the amount by which past values of a signal aid in prediction of the current values of another signal (hence an implicit notion of causation).

Multivariate autoregressive (MVAR) models extend this approach to more than two time series by predicting each of the signals based on the previous values of all other signals. Specifically, let \mathbf{X} denote a K -dimensional stochastic multivariate process of length T . In our case, \mathbf{X} corresponds to the set of $K = 60$ channels of EEG recorded over T time points. A value of this process at time instant t is the K -dimensional data vector $X(t) = (X_1(t), X_2(t), \dots, X_k(t))'$. This vector can be estimated as a regression on its p previous values (a vector autoregressive process) as:

$$X(t) = \sum_{m=1}^p \mathbf{A}_m X(t-m) + E(t) \quad (3.3)$$

Here, \mathbf{A}_m 's are $K \times K$ model coefficient matrices where $\mathbf{A}_m(i, j)$ represents the effect (weight) of sub-process X_j on X_i at lag m ; and $E(t)$ is a K -dimensional zero-mean white noise process with a non-singular covariance matrix Σ . We have assumed, without loss of generality, that $X_1(t), X_2(t), \dots, X_k(t)$, $k = 1, \dots, K$ are zero-mean sub-processes and that the same model order p is required to regress on all signals.

Relating equations 3.2 and 3.3, extension of Granger causality to more than two variables thus involves fitting an MVAR model to the data. In this context, a time series $X_i(t)$ is called a Granger cause of the time series $X_j(t)$ if at least at one lag m , $m = 1, \dots, p$, the corresponding element of the coefficient matrix $\mathbf{A}_m(i, j)$ is significantly greater than zero in absolute value sense [86], [87].

3.2.3 Autoregressive Modeling of Nonstationary Data

In practice, autoregressive models are typically restricted to stationary time series so that an accurate model fit can be realized. However, many biomedical signals, specially the EEG, are highly nonstationary in nature. There are two approaches for modeling nonstationarity EEG time series:

- I. **Segmentation:** We may assume that segments of EEG in small overlapping windows are at least quasi-stationary, so an MVAR model can be accurately fit to each of the segments. Adopting a similar concept to Short Time Fourier Transform (STFT), we therefore model local sections of a multivariate signal as it changes over time.

A problem with this approach is the concern of having sufficient data points falling within each segment. Fitting an MVAR model to a high-dimensional time series amounts to determining a large number of parameters relating each channel to lagged values of other channels. Therefore, a large number of data points are needed to have a well-posed fitting problem and this restricts our ability to choose a short window length for satisfying assumptions of quasi-stationarity. Nonetheless, fitting MVAR models to long segments of EEG has been suggested in the literature [88], [89], and can be justified as being useful in assessing the aggregate connectivity structure within each window, disregarding the transients. In section 3.4.1, we will fit models to 10-second

epochs of EEG and average the results over all epochs. This may lead us to an overview of the average connectivity structure inferred from a full-length recording during a specific task.

II. **Adaptive models:** Alternatively, we can model the nonstationary EEG using adaptive variants of the MVAR process, i.e. assuming that the model itself varies over time in accordance with the data. In this sense, the matrices \mathbf{A}_m (and hence the connectivity structure) are dependent on time and the equation 3.3 can be modified to represent instantaneous model parameters:

$$X(t) = \sum_{m=1}^p \mathbf{A}_m(t)X(t-m) + E(t) \quad (3.4)$$

This approach will capture the transient features of effective connectivity and result in *dynamic* task-specific connectivity analysis. Details regarding adaptive MVAR modeling are discussed in section 3.3.2.

Through the rest of this chapter, we have used a constant parameter matrix notation \mathbf{A} . It goes without saying that in the adaptive case, this matrix (and its corresponding variants) can be implicitly substituted with $A(t)$, its instantaneous value at time t .

3.2.4 Representation in Frequency Domain

The formulation in section 3.2.2 can be transformed to the frequency domain to study couplings in different frequencies, as is common with EEG analysis. Specifically, rearranging 3.3 and assuming $\hat{\mathbf{A}}_0 = I$ and $\hat{\mathbf{A}}_m = -\mathbf{A}_m$,

$$E(t) = \sum_{m=0}^p \hat{\mathbf{A}}_m X(t-m). \quad (3.5)$$

Transforming 3.5 into the frequency domain, we get

$$\mathbf{E}(f) = \mathbf{A}(f)X(f) \quad (3.6)$$

$$\mathbf{A}(f) = \sum_{m=0}^p \hat{\mathbf{A}}_m \exp(-2\pi i m f / f_s) \quad (3.7)$$

where f_s is the sampling frequency. 3.6 can also be rearranged in the following form:

$$X(f) = \mathbf{A}^{-1}(f)\mathbf{E}(f) = \mathbf{H}(f)\mathbf{E}(f) \quad (3.8)$$

Equation 3.8 suggests that the AR approach models the process \mathbf{X} as a filter acting on the white noise process \mathbf{E} . Since the spectrum of white noise is flat over all frequencies, information about the spectral content of \mathbf{X} is contained in the matrix $\mathbf{H}(f) \triangleq \mathbf{A}^{-1}(f)$, also known as the transfer matrix. From the transfer matrix $\mathbf{H}(f)$ and the prediction error covariance matrix Σ , the spectral density matrix \mathbf{S} of the process can be calculated as

$$\mathbf{S}(f) = \mathbf{X}(f)\mathbf{X}^*(f) = \mathbf{H}(f)\mathbf{E}(f)\mathbf{E}^*(f)\mathbf{H}^*(f) = \mathbf{H}(f)\Sigma\mathbf{H}^*(f) \quad (3.9)$$

where $*$ denotes complex conjugation. As we shall see in the following section, matrices $\mathbf{S}(f)$, $\mathbf{H}(f)$, and $\mathbf{A}(f)$ derived from the EEG process carry information about directed connectivity, and several quantitative connectivity metrics have been defined in the literature based upon these matrices, each targeting a different aspect of information flow.

3.2.5 Frequency Domain Estimators of Directed Connectivity

Here we introduce and define a selection of quantitative metrics for effective connectivity in a coherence and/or Granger-causal sense, derived from the matrices defined in the previous sub-section. Our goal is not to provide a comprehensive review on these measures, so the list goes well beyond the few measures introduced herein.

- **Coherency (Coh):** Perhaps the simplest measure of coupling in the frequency domain is Coherency, defined in terms of the spectral matrix \mathbf{S} as

$$C_{ij}(f) = \frac{S_{ij}(f)}{\sqrt{S_{ii}(f)S_{jj}(f)}} \quad (3.10)$$

Coherency measures the degree of synchrony among the subprocesses at different frequencies and is not a directional measure. The directional versions

of coherency, such as Directed Coherence [90] are limited to bivariate models and do not fully consider the multivariate nature of the process [91].

- **partial Coherence (pCoh):** In a multivariate process, coherence between two subprocesses might be influenced by all other variables. The Partial Coherence [92], [93] attempts to find the portion of coherence between two subprocesses which cannot be explained by a linear combination of other common inputs. Partial Coherence is defined as:

$$P_{ij}(f) = \frac{M_{ij}(f)}{\sqrt{M_{ii}(f)M_{jj}(f)}} \quad (3.11)$$

where M_{ij} is a minor determinant of \mathbf{S} with the i -th row and j -th column removed. It can be shown [94] that (3.11) is equivalent to

$$P_{ij}(f) = \frac{\hat{S}_{ij}(f)}{\sqrt{\hat{S}_{ii}(f)\hat{S}_{jj}(f)}} \quad (3.12)$$

where $\hat{\mathbf{S}}(f) = \mathbf{S}^{-1}(f)$.

- **Partial Directed Coherence (PDC):** Another estimator based on the matrix $\mathbf{A}(f)$, the Partial Directed Coherence (PDC), has been proposed in [95]. PDC is defined in terms of the coefficient matrix \mathbf{A} as:

$$\pi_{ij}(f) = \frac{A_{ij}(f)}{\sqrt{\sum_{k=1}^K |A_{kj}|^2}} \quad (3.13)$$

The complex quantity $\pi_{ij}(f)$ can be interpreted as the causal flow from channel j to channel i normalized by all outflows from channel j . Since it is based on the values A_{ij} (the parameters of the MVAR model), PDC can be viewed as a frequency-domain equivalent of multivariate Granger causality [96].

- **Directed Transfer Function (DTF):** Similarly to PDC, the Directed Transfer Function (DTF) [84] is a multivariate directional measure defined based

on the elements of the transfer matrix \mathbf{H} as

$$\gamma_{ij}^2(f) = \frac{|H_{ij}(f)|^2}{\sum_{k=1}^K |H_{ik}(f)|^2} \quad (3.14)$$

γ_{ij}^2 represents the directional flow from channel j to channel i normalized by the sum of flow from all channels to channel i . The normalization in the original definition of DTF (3.14) is done in order to compare directed components in signals with different power spectra [97]. However, DTF can also be defined in a simpler, non-normalized format as:

$$\theta_{ij}^2(f) = |H_{ij}(f)|^2 \quad (3.15)$$

It is argued in [86] that DTF does not represent Granger Causality. Rather, DTF and Granger causal tools such as PDC focus on different and complementary aspects of the connectivity structure.

- **full-frequency Directed Transfer Function (ffDTF)**: Integrating the denominator in (3.14) over frequency leads to a variant of DTF, full-frequency DTF (ffDTF) [98]:

$$\lambda_{ij}^2(f) = \frac{|H_{ij}(f)|^2}{\sum_f \sum_{k=1}^K |H_{ik}(f)|^2} \quad (3.16)$$

Compared to DTF, ffDTF allows for better interpretation of the estimator characteristics at different frequencies.

- **direct Directed Transfer Function (dDTF)**: DTF and its variants show not only direct but also indirect, mediated interactions [98]. For instance, if two non-interacting channels A and B are influencing channel C such that $A \rightarrow C$ and $B \rightarrow C$, then DTF will falsely detect the indirect interaction $A \rightarrow B$. A more robust variant of DTF that is able to distinguish between direct and indirect flows among channels is introduced in [98] as the product of full-

frequency DTF and partial coherence:

$$\begin{aligned}\delta_{ij}^2(f) &= \lambda_{ij}^2(f) P_{ij}^2(f) \\ &= \frac{|H_{ij}(f)|^2}{\sum_f \sum_{k=1}^K |H_{ik}(f)|^2} \times \frac{(\hat{S}_{ij}(f))^2}{\hat{S}_{ii}(f) \hat{S}_{jj}(f)}\end{aligned}\quad (3.17)$$

Direct DTF (dDTF) is thus a multivariate directional measure which combines information from both DTF and Partial Coherence.

A comparison of some of the measures introduced above is presented in [99], where it is concluded that all measures perform nearly equivalently under reasonable recording conditions. In this thesis, we proceed with dDTF as our measure of effective connectivity since it has the combined advantages of ffDTF and Partial Coherence.

3.3 Workflow, Methods, And Practical Considerations

In section 3.2 we outlined the theory underlying Granger-causal analysis and introduced a number of connectivity estimators. We concluded that we can estimate effective connectivity in multi-channel EEG using an approach based on linear Multivariate Autoregressive models; and that this approach can be used adaptively to infer instantaneous connectivity patterns. The detailed procedure for obtaining an estimate of the connectivity structure from raw EEG data is depicted in Figure 3.1. In the following, we will discuss methods and practical issues related to each step of the procedure.

3.3.1 Pre-processing And Artifact Removal

The first step is to remove artifacts from the data as outlined in section 2.2.1, though more stringent criteria need to be exercised for removal of artifacts. In other words, contrary to the previous chapter, here we also reject, as much as possible, portions of data corresponding to blinks and low-frequency artifacts as they affect and distort the parameters of the MVAR model, especially in the adaptive, time-varying case.

Extra caution needs to be exercised in pre-processing of the EEG for estimation

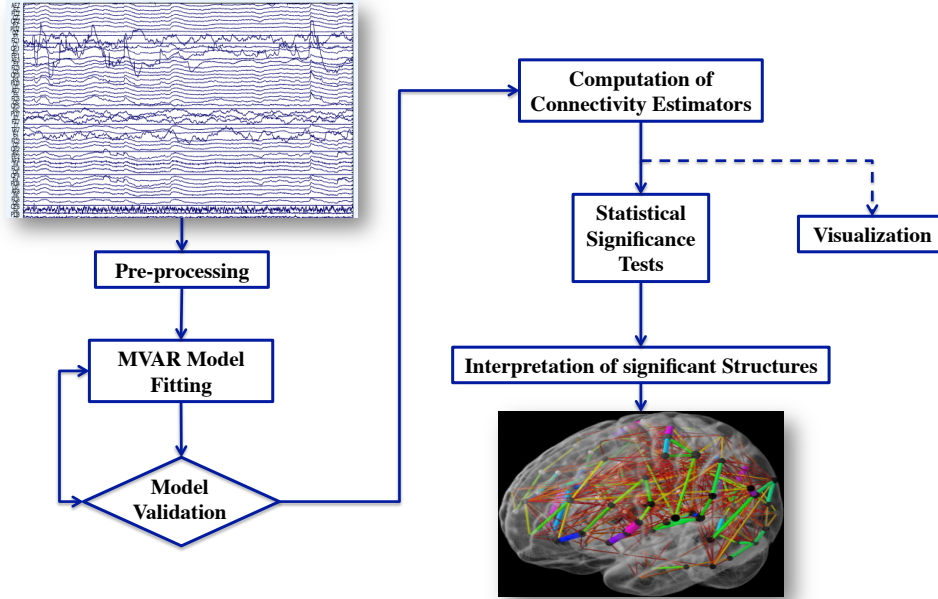


Figure 3.1: From raw time series to connectivity patterns: steps for estimating effective connectivity based on multivariate autoregressive models

of the connectivity measures. Since these measures are dependent on the signal phase, any filtering with phase distortion would invalidate the final results. Re-referencing is another procedure that would distort the estimates, as the choice of reference is shown to have a significant impact on the derived network attributes [100], and average-rereferencing mixes the signals and introduces false correlations between them. We thereby chose to have as little pre-processing steps as possible, bypassing the conventional pre-filtering steps. We do, however, normalize every channel by removing the mean and dividing by the standard deviation according to the Equation (3.18) below prior to segmentation and MVAR modeling:

$$x_k^{norm}(t) = \frac{x_k(t) - \overline{x_k(t)}}{\sigma_k}, \quad k = 1, \dots, K \quad (3.18)$$

where $\overline{x_k(t)}$ and σ_k refer to the temporal mean and the temporal standard deviation of the signal at electrode k , respectively. Since many of the connectivity measures described in section 3.2.5 are highly dependent on scale and variances of the signals, this step is performed to scale the variances among different signals to a comparable range in order to prevent model misspecifications.

3.3.2 Model Fitting And Validation

Having ensured that the data is free of artifacts, the next step would be to fit an MVAR model to the time series. Model fitting refers to implementation of an algorithm for computing the coefficient matrices \mathbf{A}_m , $m = 1, \dots, p$ and the error covariance matrix Σ (See Equation 3.3) given the process time series \mathbf{X} collected over T time points. Here we discuss our choice of the fitting algorithm and the criterion for choosing the model order p .

The Model Fitting Algorithm

As discussed in section 3.2.3, there are two approaches for MVAR modeling of nonstationary EEG time series: 1) Segmentation, which results in batch-averaged connectivity estimation, and 2) Adaptive MVAR modeling, resulting in instantaneous (dynamic) connectivity estimation.

Static MVAR models can be fitted to a batch of signals falling within a window using various methods including least-squares (Yule-Walker) approaches, Burg's method, and the Vieira-Morf algorithm. In this thesis, we have used an efficient step-wise least squares method proposed in [101] and [102]. The only consideration here is the choice of the window length, which is dependent upon the minimum analysis frequency and the number of parameters of the MVAR model. We chose the window length to be 10 seconds as in [88] and [89]. Considering the estimation problem, there are $K^2 p$ free parameters to estimate in an MVAR model and as a rule of thumb, at least 10 times more data samples are needed for an accurate estimation ([51]). With a generic order of $p = 8$, we have $60^2 * 8 \approx 29000$ parameters to estimate and we need at least 290000 data points, which are provided in a 10-second window ($60(\text{channels}) * 500(\text{Hz}) * 10(\text{s}) = 300000$). Therefore, the selected window length of 10 s seems to be a reasonable choice. We have also

included an overlap of 50% (5 seconds) between windows in order to have more batches of available data as well as a smoother distribution of connectivity parameters.

In addition to batch-based models, adaptive MVAR models are estimated using the Recursive Least Squares (RLS) algorithm with forgetting factor [103]. The RLS algorithm was preferred over methods such as Kalman filtering due to being better suited for high-dimensional data. Specifically, in Kalman-filter based approaches, the required matrix inversions cannot be avoided [103] and this is especially undesirable in cases when the dimension of the time series is large. Also, it is shown in [103] that the model dimension has no influence on the RLS algorithm's adaptation speed and its estimation properties. The only tuning parameter of the algorithm, the forgetting factor, represents the trade-off between adaptation speed and the variance of the estimation (this parameter was empirically set to 0.002 and was fixed throughout all recordings).

Choice of the Model Order

In an autoregressive model, the order p is the number of lags used for regression on the previous process values. Since the order is not known a priori, we need a data-driven criterion that would determine an optimal value for p given the multivariate time series. The most popular methods to this end are information-theoretical approaches such as Akaike's Final Prediction Error (FPE) [104], and the Schwarz Bayesian Criterion (SBC) [105]. Generally, these methods attempt to minimize an entropy-based objective function comprising of a prediction error term and a penalty term for including too many parameters (large model orders). By minimizing both terms over a range of model orders, they search for an order which is optimal in the sense that it is both parsimonious and that it predicts the data well.

The FPE and SBC methods function rather conservatively and impose too high a penalty for large model orders; that is, when used on a 10-second segment of our EEG data, FPE and SBC criteria yield optimal orders of 3 and 1 respectively, which are likely too low for accurate spectral identification. Therefore, we have used a rather heuristic approach for picking a proper model order. This approach is based on the fact that if the model is accurately representative of the data, the correlation

structure of the data will be completely described by the model. Hence the residuals $\mathbf{U}(t) = \mathbf{X}(t) - \sum_{m=1}^p \hat{\mathbf{A}}_m \mathbf{X}(t - m)$ should not exhibit significant correlation, and validating the model amounts to checking the whiteness (uncorrelatedness) of its residuals. This can be assessed by computing cross-correlations of the residuals up to some maximum lag, and checking whether they will be sufficiently small with the current choice of the model order.

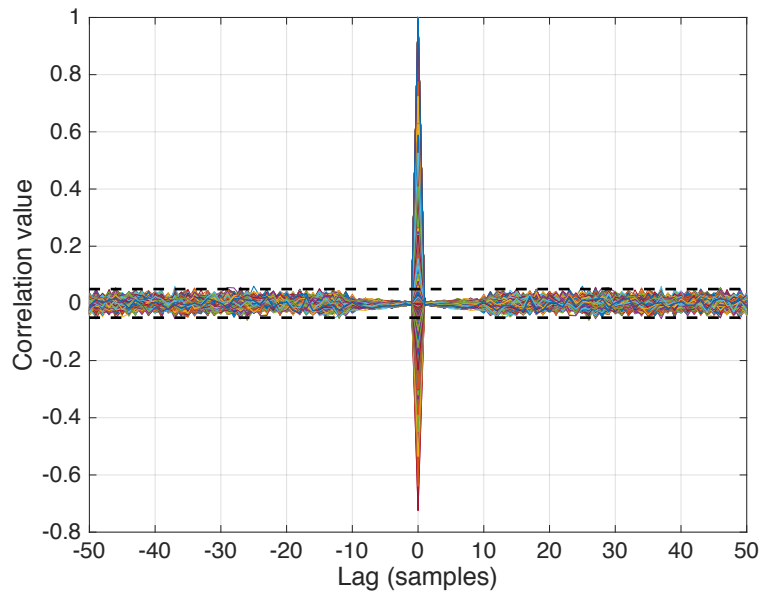


Figure 3.2: Normalized auto and cross-correlations among all 60 channels of the model residuals

We found that a model order $p = 10$ is enough to keep the normalized covariance of the residuals reasonably small. Figure 3.2 depicts the correlation structure of the residuals of a model with $p = 10$ fitted to a 10-second segment of the data (the 60^2 autocovariance and cross-covariance sequences for all combinations of the residual dimensions are overlaid on the same plot). We observe that with $p = 10$, residual correlations will be bounded by ± 0.05 for all lags other than zero. Hence, we may claim that with %95 confidence, the residuals are white and the model is valid. We have also empirically assumed that this choice of the optimal model order is sufficient to keep the residuals white among all of the recordings. Based

on this observation, the order was also kept fixed at $p = 10$ for dynamic MVAR modeling in the RLS algorithm.

3.3.3 Computation of Connectivity Estimators

Once we have fitted a valid MVAR model to the data, we may proceed to computing the quantitative measures of effective connectivity described in section 3.2.5 from the parameters of the model. As shown in section 3.2.2, fitting MVAR models to the time series data would result in K -by- K parameter matrices A_m , $m = 1, \dots, p$. These parameter matrices are then transformed to the frequency domain (Equation 3.7) to yield arrays of the form $\mathbf{A}(f)$ ($K \times K \times N_t \times N_f$), where

- N_t is, for the static connectivity case, the number of overlapping windows (segments) extracted from the whole length of the recording; whereas in the dynamic connectivity case N_t is the number of discrete time samples;
- N_f is the number of discrete frequency values at which $\mathbf{A}(f)$ is evaluated.

These four-dimensional arrays encapsulate the model parameter information in terms of time (or epoch), frequency, and channel-wise interactions. Once computed, they are passed to functions calculating the connectivity estimators explained in section 3.2.5, which in turn yield connectivity arrays of a similar form \mathbf{C} ($K \times K \times N_t \times N_f$). As a case in point, assuming we have calculated the connectivity measure DTF (Equation 3.15), the element (i, j, t, f) in the connectivity array \mathbf{C} represents the causal interaction of channel j on channel i at time t and frequency f as measured by the metric DTF.

An issue arising in computation of dynamic (time-dependent) connectivity structures is that these arrays can easily become so large that they exceed the available computer memory and cause programs to be unresponsive. For instance, when calculating the time-varying dynamic connectivity of 10 seconds of data in 50 frequency points, the connectivity array will take up to $60 \times 60 \times 10 \times 500(F_s) \times 50 \times 8(\text{bytes per array element}) = 7200$ megabytes in memory. Considering the fact that these arrays are to be further manipulated through the rest of the program and compared among conditions and subjects, they are impractical to use unless somehow compressed and reduced. To this end, we have eliminated the third dimension

(frequency) by integrating the measures over frequency in the bands of interest. Moreover, in this thesis, we have examined the time-varying connectivity structure only during a short period of time after the beginning of performing a task (usually the first 5 seconds).

3.3.4 Tests for Statistical Significance

Proper interpretation of connectivity patterns is not achievable without a suitable statistical testing scheme which is able to distinguish significant interactions from insignificant ones. Specifically, we have seen that computation of any connectivity estimator on a segment of EEG at a particular time and frequency yields K^2 values, each corresponding to the directional flow from one channel to another. These values often need to be compared between two conditions and assessed among subjects to infer significant and consistent patterns. Similar to our approach in the previous chapter, we have compared pair-wise connectivity values during each task to those of the resting state. In this sense, a task-specific connection from channel A to channel B is deemed significant if and only if its connectivity value is greater (in a statistical sense) than that of the resting state. Our methods for statistical testing are customized to the static and dynamic connectivity estimation as follows:

- In the case of static connectivity, we are comparing frequency-integrated arrays $C_{rest}(K \times K \times N_{rest})$ and $C_{task}(K \times K \times N_{task})$. Each directed pair of channels has N_{rest} realizations (hence a 'distribution' of connectivity values) in the resting state and N_{task} realizations during performance of the task (Figure 3.3a). For each directed pair of channels, we can therefore compare means of the two distributions for the rest and task conditions using a Wilcoxon signed rank test. Once the means of all resting-state batches are compared with those of the task state, a $K \times K$ 'significance matrix' \mathbf{S} of zeros and ones is derived in which $\mathbf{S}(i, j) = 1$ implies that for the interaction from channel j to channel i , the mean connectivity value during task is significantly greater than the mean connectivity value during rest, and hence the connection from j to i is task-specific. By comparing the means of the two distributions, we are essentially examining the time-averaged (or more specifically, batch-averaged) connectivity over all epochs of the rest and task

recordings.

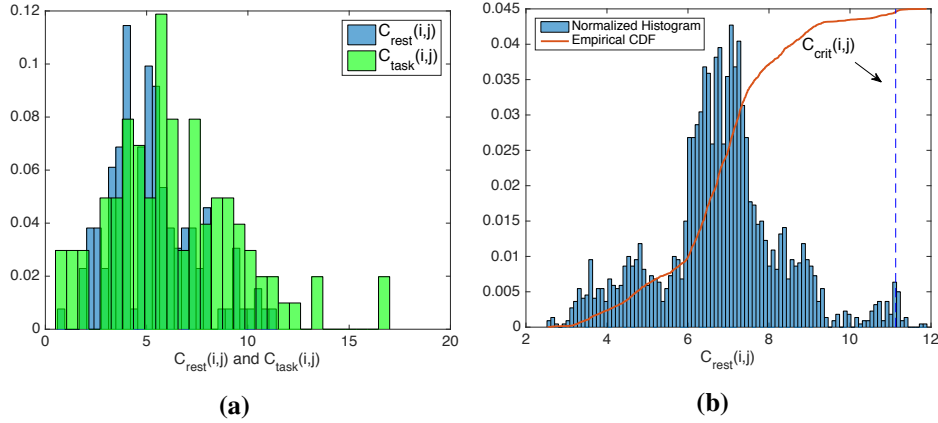


Figure 3.3: Our statistical significance testing method for determination of significant pair-wise interactions. The directed pair whose connectivity values are depicted above are $FC2$ and $F3$, with $C(i, j)$ signifying the directed interaction $FC2 \rightarrow F3$. (a) In static connectivity estimation, all values of pair-wise interactions at rest are compared with those during task in an offline manner; (b) In dynamic connectivity estimation, instantaneous values of interactions during task are compared with a critical value obtained from the cumulative distribution of all resting-state values.

- As for dynamic connectivity, significant interactions need to be identified at every instant throughout the length of the recording. Hence, pair-wise distributions of rest and task connectivity values cannot be assessed in an offline manner that leads to loss of temporal information. Rather, we may gather all resting-state connectivity realizations (at all time instants) into a 'baseline distribution', and examine at what point in time the connectivity value during a task is exceeding a 'critical' value (Figure 3.3b). In this context, the critical connectivity value $C_{crit}(i, j)$ for each directed pair of channels is defined as the value at which the cumulative distribution of resting-state connectivity values reaches $1 - \alpha$, where α is some significance level. Essentially, significant connectivity values during a task are values which are unlikely to occur during rest; and that is the rationale behind looking at the

tail of the resting-state distribution. The significance matrix \mathbf{S} in this case would be of size $K \times K \times N_t$ and would comprise of the instantaneous significant interactions evolving over time.

It is worth mentioning that simultaneous comparison of a large number of interactions will raise the chances of occurrence of type 1 errors. Hence, the significance level needs to be corrected and set to a more conservative value to decrease the number of false-positive significant interactions. We have used the Bonferroni correction method for this purpose, i.e. lowered the significance level from α to α/K^2 .

3.3.5 Visualization and Further Data Reduction

So far, we have fitted MVAR models to batches or instants of the time series, computed the connectivity metrics, and assessed the statistical significance of these metrics. At this point, we need to be able to visualize and interpret a vast number (i.e. 60^2) of significant and insignificant interactions that may or may not differ among subjects and even different instances within the same recording. Visualization of a connectivity structure is not an easy task, especially when the number of electrodes is large and in scenarios like ours where the notion of direction needs to be preserved by the visualization method.

Perhaps the most readily available visualization scheme is to plot the significance matrix as an image, such that each pixel corresponds to a directed pair-wise interaction and its color indicates whether or not the interaction is significant. Figure 3.4 depicts such an image obtained from comparison of gamma band static connectivity between the ankle movement and rest conditions for subject 1. Even though a few high-level features can be identified from this figure (see section 3.4), it contains too much detail to be informative of the overall connectivity structure in the first glance. Moreover, the significance matrix changes instantly in the dynamic scenario, making it extremely difficult to follow the patterns. There is thus an inevitable need to reduce this information and represent it in a compact and more interpretable manner.

To this end, we may utilize the same approach as in section 2.3.2 for further reducing the significance matrix, i.e. grouping the neighboring electrodes into nine

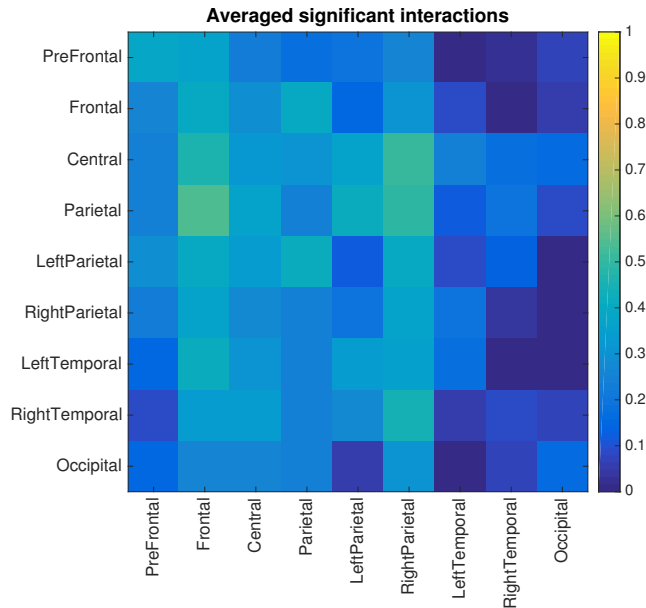


Figure 3.5: Reduction of Figure 3.4 by averaging channel interactions within the brain regions specified in table 2.1, where the average is taken over all directed channel pairs (e.g. the regional interaction value from region i to region j is calculated by taking the average of all $N_i \times N_j$ pairwise connectivity values between the two regions, where N_i and N_j are, respectively, the number of channels in regions i and j). Each colored block represents the average strength of directional connections from the region below the block to the region on its left. For illustrative and comparison purposes, interaction matrices are normalized to have unit Frobenius norm.

of boundaries, neighboring electrodes do not always fall into the same group (e.g. in Figure 2.4, channels FC4 and FC6 are immediate neighbors, but belong to two distinct groups). In other words, 'spatial discretization' of the electrodes does not take into account the interactions between adjacent electrodes near the boundaries, resulting in a relatively smeared representation of regional interactions.

Graph-theoretical Measures

In order to overcome these limitations and further reduce the high-dimensional data for visualization (especially in the case of dynamic connectivity patterns), we may

turn to graph theory. The main idea behind graph-theoretical measures is that large connectivity datasets have the same characteristics as 'networks' emerging in biology, economy, internet, and other fields; and their properties can be characterized as holistic, compact, meaningful, and easily computable network measures. Graph theory is a field of mathematics defined to study these networks and their properties and has been extensively used in the past decade for the analysis of brain networks [106].

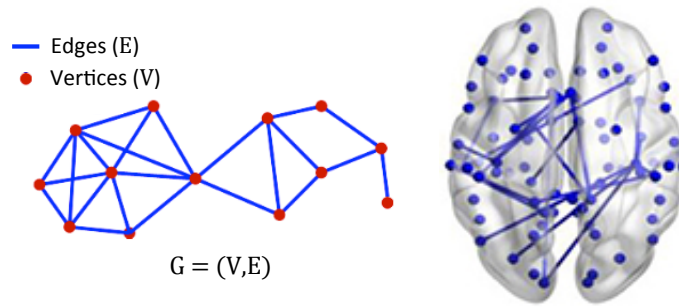


Figure 3.6: A graph G (shown on the left) is an inter-connected set of vertices (V) and edges (E). Brain networks can be represented as graphs. The non-causal connectivity network depicted on the right can be obtained by thresholding the connectivity values and discarding their direction.

In mathematics, a graph is a structure consisting of a set of 'nodes' having some sort of inter-connections represented as 'edges' (Figure 3.6). In the context of brain networks, nodes represent channels and edges represent the strength (or presence) of the connectivity measures. Once the computed connectivity structure is defined in terms of a graph, features of the network can be summarized in terms of quantitative graph-theoretical measures such as centrality, clustering coefficient, efficiency, path length etc. [106]. In this thesis, we have used a few basic graph-theoretical measures that are outlined below; including inflow, outflow, and causal asymmetry ratio [107]. Denoting the computed connectivity measure from channel j to channel i by c_{ij} ,

- **Inflow** (I_i) is defined as the sum of causal information flowing from the rest of the system toward channel i : $I_i = \sum_{j=1}^K c_{ij}$,

- **Outflow** (O_j) is defined as the sum of causal information flowing from channel j toward the rest of the system: $O_j = \sum_{i=1}^K c_{ij}$,
- **Causal Asymmetry Ratio** (CAR_i) is a normalized value indicating asymmetry of information flowing in and out of channel i : $CAR_i = \frac{O_i - I_i}{O_i + I_i}$.

Based on definitions above, a high value of outflow indicates that the channel acts as a source (causally influencing the system), and channels having high inflow values acts as sinks (being causally influenced by the system). The causal asymmetry ratio has values ranging from -1 to 1 , with positive values close to 1 indicating source behavior and negative values close to -1 suggesting that the channel influences the system more as a sink. A CAR value around zero would indicate that the channel is relatively passive in that the amount of influence it imposes on the network is equalized by the amount of influence it receives from the network.

Since these measures are summing the pairwise connectivity values to obtain channel-wise values, they essentially reduce the dimensionality of the connectivity structure from K^2 to K . In addition to being compact, these measures are intuitive and neurologically insightful. They can easily be computed and visualized on a topographical plot, circumventing the enforced abstraction of location information (as in Figures 3.4 and 3.5) and hence simplifying visualization of the directed connectivity structure.

3.4 Results And Discussion

Having laid the foundations and a framework for estimation of effective connectivity, we now present the results of applying this framework to the data at hand. For simplicity and based on results from the previous chapter, we only consider motor tasks for connectivity estimation and will analyze the rest of our data in future publications.

We begin by presenting the results of batch-averaged (static) connectivity in section 3.4.1. To clarify and sum up, the results presented in section 3.4.1 are obtained by:

1. cleaning the raw recordings by rejecting artifactual channels (yielding $K' < K$ clean channels per recording) and rejection of transient artifactual time

segments,

2. extracting 10-second epochs with 50% overlap from clean rest and task recordings (usually, around 130 rest epochs and 30 task epochs are extracted per subject),
3. fitting an MVAR model ($p = 10$) to each epoch, calculating the epoch dDTF measure (Equation (3.17)), and integrating the dDTF values in the gamma band,
4. statistically comparing the motor dDTF values with those of the resting state (section 3.3.4) and obtaining the $K \times K$ pair-wise significance matrices per subject, where values corresponding to the rejected channels are left empty¹,
5. averaging the $K \times K$ pair-wise significance matrices (ignoring empty values) across subjects to determine significant dDTF connections which are common to all subjects and hence survive averaging.

Steps 4 and 5 above outline our strategy for group-level (between-subjects) analysis: we first obtain subject-specific significance matrices by statistically comparing the two conditions for each individual subject. This procedure rules out, for each subject, any connection which is not task-specific. Subsequently, group-level results are obtained by averaging these significance matrices across subjects. Averaging promotes general trends among all subjects by preserving common connections and suppressing connections which are specific only to a single subject.

Next, results from dynamic connectivity analysis are presented in section 3.4.2. Similarly, these results have been obtained by:

1. cleaning the raw recordings by rejecting artifactual channels and transient artifactual time segments,
2. extracting the first 5 seconds from the rest and task recordings per subject,

¹In MATLAB, empty matrix values are implemented as NaN, the IEEE arithmetic representation for Not-a-Number.

3. fitting an instantaneous MVAR model ($p = 10$) using the RLS algorithm, calculating the dDTF measure at each instant, and integrating the instantaneous dDTF values in the gamma band,
4. statistically comparing the instantaneous motor dDTF values with the overall resting state values and obtaining the $K' \times K'$ pair-wise significance matrices for all time instants.

For reasons explained in section 3.4.2, dynamic connectivity is not analyzed on a group-level basis and is inspected for all subjects individually.

3.4.1 Static Connectivity Results

Figure 3.7 depicts the significance matrices of three subjects in both environments for one of the motor tasks (ankle movements). Although somewhat too detailed, a number of overall structural properties can be deduced from these figures.

First, in many cases, one or more well-defined columns of the significance matrix with connections to most of the channels can be seen. These columns represent prominent sources of information flow and can be useful in identification of 'critical nodes' in the network. However, we observed that these sources are not consistent as they differ among subjects, and even among different recordings of the same subject. They are thus not reported here in isolation, but re-examined shortly using Graph-theoretical measures.

Interestingly, we also observe that for a specific subject, more significant connections are present in recordings at LSBB than their counterparts at the hospital environment. This is a direct consequence of low-noise conditions, and is in accordance with our findings in section 2.3.2, as task-specific effective connectivity is another gamma band correlate which is enhanced and better detected in the low-noise environment.

Another property deducible from Figure 3.7 is laterality and the amount of inter and intra-hemispheric connections. Based on the arrangement of electrodes depicted in detail in Figure 3.4, and the 10-10 montage shown in Figure 2.4, entries in a significance matrix can be classified according to the corresponding hemispheres they are connecting. Figure 3.8 below shows a mapping of all of the pixels to their

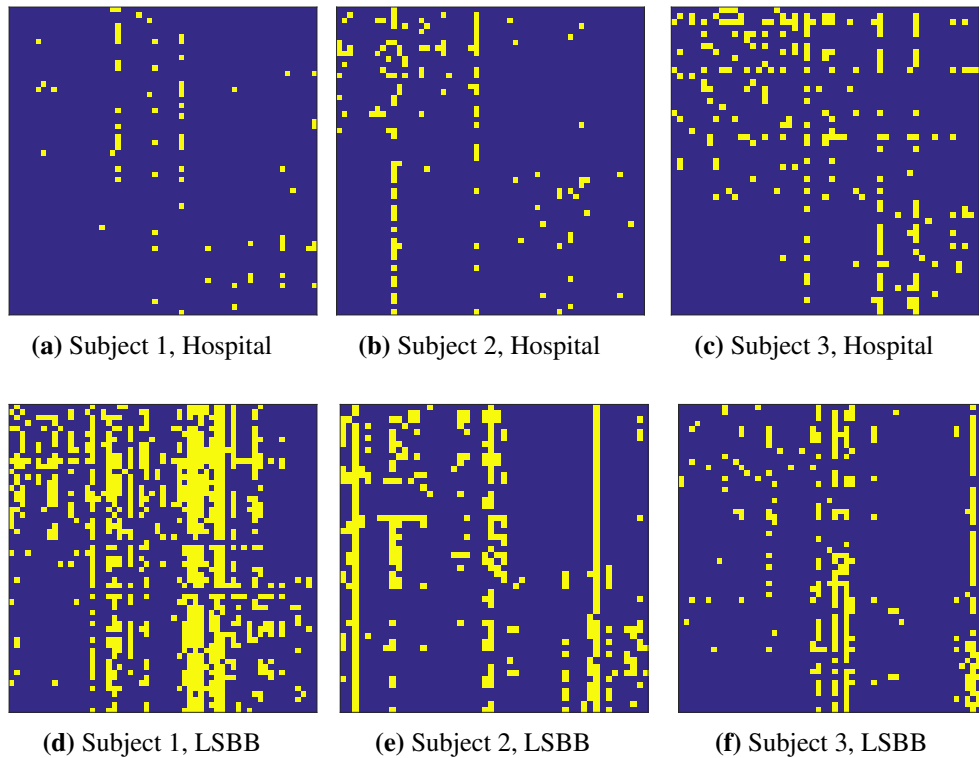


Figure 3.7: Significant connections during ankle movement from three subjects in the two environments (chosen arbitrarily from the four subjects common to both environments). Electrode labels are not shown on the axes, as the overall structures are the main point of notice. 'Global' sources of activity, i.e. channels with connections to the majority of other channels are evident in subfigures (d) and (e); while more local sources, connected only to a subgroup of electrodes, can be spotted in other subfigures.

corresponding inter and intra-hemispheric connections. This crude classification of electrodes leads to the observation that on average, there are more connections within the same hemisphere than between hemispheres, since the yellow pixels (significant connections) are more densely distributed in the top-left and bottom-right corners of the images in Figure 3.7.

In Figure 3.9 we have quantified the inter and intra-hemispheric connections across all of the significance matrices, as well as those corresponding to wrist

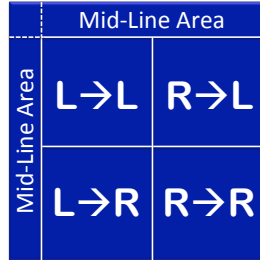


Figure 3.8: Segmentation of significance matrices into hemispheric connections. This particular arrangement stems from the ordered sequence of electrodes in Figure 3.4, having the mid-line electrodes first (names ending in 'Z'), electrodes in the left hemisphere second (names ending with an odd number), and lastly, electrodes in the right hemisphere (names ending with an even number). $L \rightarrow L$ denotes connections within the left hemisphere, $L \rightarrow R$ denotes connections from the left hemisphere to the right, and so on.

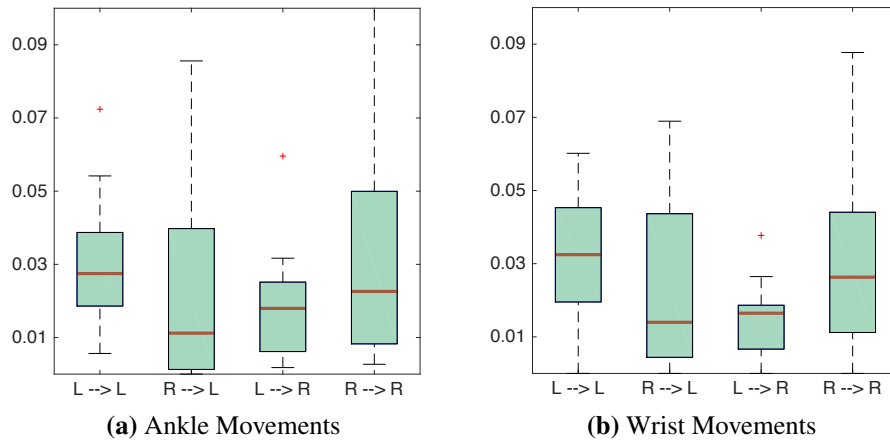
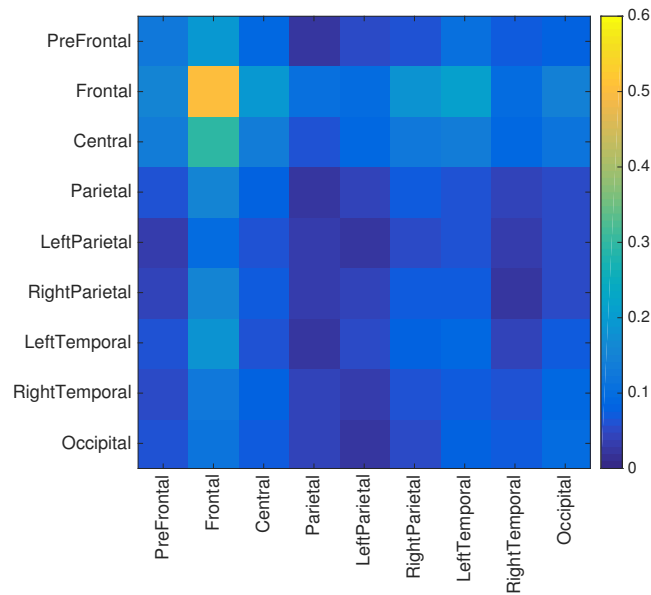


Figure 3.9: Overall strengths of inter and intra-hemispheric task-specific connectivity during motor tasks in eight subjects and two environments. Box plots represent the median and quartiles of the distribution of hemispheric strength values across all subjects in both environments. Each strength value is essentially the number of significant connections from one hemisphere to the other, divided by the total number of significant connections.

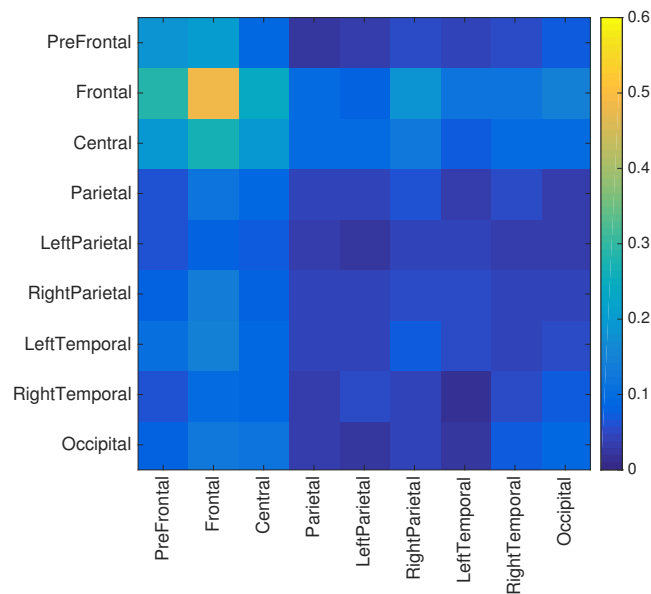
movements. Each entry is the result of calculating the ratio of significant interactions to the total number of possible interactions within the regions designated in Figure 3.8, discarding the pixels falling in the mid-line areas. The figure confirms our previous observation that the number of significant intra-hemispheric connections is more than the number of inter-hemispheric connections. The overall number of connections is also shown to be slightly higher in the left (contralateral) hemisphere than in the right. This suggests that, in a Granger-causal sense, the contralateral hemisphere is more gamma-band-inter-connected during ankle and wrist movements than the ipsilateral hemisphere. Further, there is seemingly more left-to-right connectivity than from the right hemisphere to the left during both ankle and wrist movements. Left-to-right connections are also less variable (as measured by the inter-quartile range of their distribution) among different subjects than other inter and intra-hemispheric connections. They might therefore be deemed, with relatively higher confidence, as subject-independent movement correlates. However, these observations may vary if more subjects are added to the analysis.

To further assess which local regions of the brain contribute the most to the task-specific connectivity structure, we can count the number of significant interactions within the brain regions specified in Figure 2.4. In Figure 3.10, we have illustrated the mean region-wise significant interactions averaged over all of the recordings (the process is explained in section 3.3.5). Figure 3.10a demonstrates that during ankle movements, frontal and central regions have the most inter-relations relative to other sites of the brain, with frontal-to-frontal and frontal-to-central activities being the most prominent region-wise interactions. In contrast, the mid- and left parietal regions are relatively less active in the connectivity process, while there is noticeable information flow from the right parietal and left temporal regions to the frontal region. Figure 3.10b shows the same characteristics for the wrist movements, although the overall connectivity pattern seems to be more structured and focused around the frontal and central areas compared to ankle movements (i.e. connections between other areas are sparser and connections between frontal and central areas are stronger).

More accurate and interpretable results are obtained using the Graph-Theoretical (GT) measures described in section 3.3.5. We begin by computing the average of significance matrices across all subjects and environments. We will then compute



(a) Ankle Movements



(b) Wrist Movements

Figure 3.10: Average regional interactions during motor tasks in eight subjects and both environments. We have recorded the number of significant interactions between the nine previously defined regions of the brain, in an attempt to represent the data in Figure 3.7 in a more compact manner, and extend the analysis of hemispheric connections.

the channel-wise GT measures of inflow, outflow, and Causal Asymmetry Ratio on the average significance matrix. The resulting GT values can then be shown on topographical scalp plots, allowing for a more intuitive representation of significant sources and sinks of information flow. Figure 3.11 illustrates the results for significant gamma band activity, averaged over recordings from eight subjects, for both of the motor tasks.

According to Figure 3.11a, on average, a cluster of frontal electrodes on the right hemisphere (F4, F6, FC2) as well as another cluster of parietal electrodes on the left hemisphere (P5, CP5) are identified as the most prominent sources of gamma band activity during ankle movement. These sources propagate information within the gamma band to the central and posterior parts of the brain on the left hemisphere, most notably to the fronto-central and parietal nodes such as FC1, C5, CP1, CZ, and PZ. Meanwhile, Figure 3.11b shows a similar structure for wrist movements, with dominant pre-frontal and parietal sources slightly shifted toward the midline in comparison with ankle movements. An interesting observation is that for both of the motor tasks, almost all channels with high values of inflow (sinks of information) are located on the contralateral hemisphere and clustered around fronto-central and parietal regions. On the other hand, sources of gamma band activity exist on both hemispheres, feeding information to the rest of the system while being organized in the form of several separate clusters on fronto-central (on the right hemisphere) and parietal (on the left hemisphere) regions of the brain.

It is argued in [108] that gamma band activity in the prefrontal cortex is linked to the maintenance of the behaviorally relevant items. This can explain the observed prefrontal sources of gamma band during the motor activity, as they could be responsible for planning of the next repetitive movement. This information then drives the specific part of the brain known to be responsible for motor function, namely, the central nodes within the contralateral hemisphere, in order to perform the act of movement. It is important to stress here that the confidence of these conclusions is confined by the limited number of subjects in the study, as the objective of this thesis was not to reach rigorous neurological discoveries, but rather to report the results on available data as a pilot gamma band study.

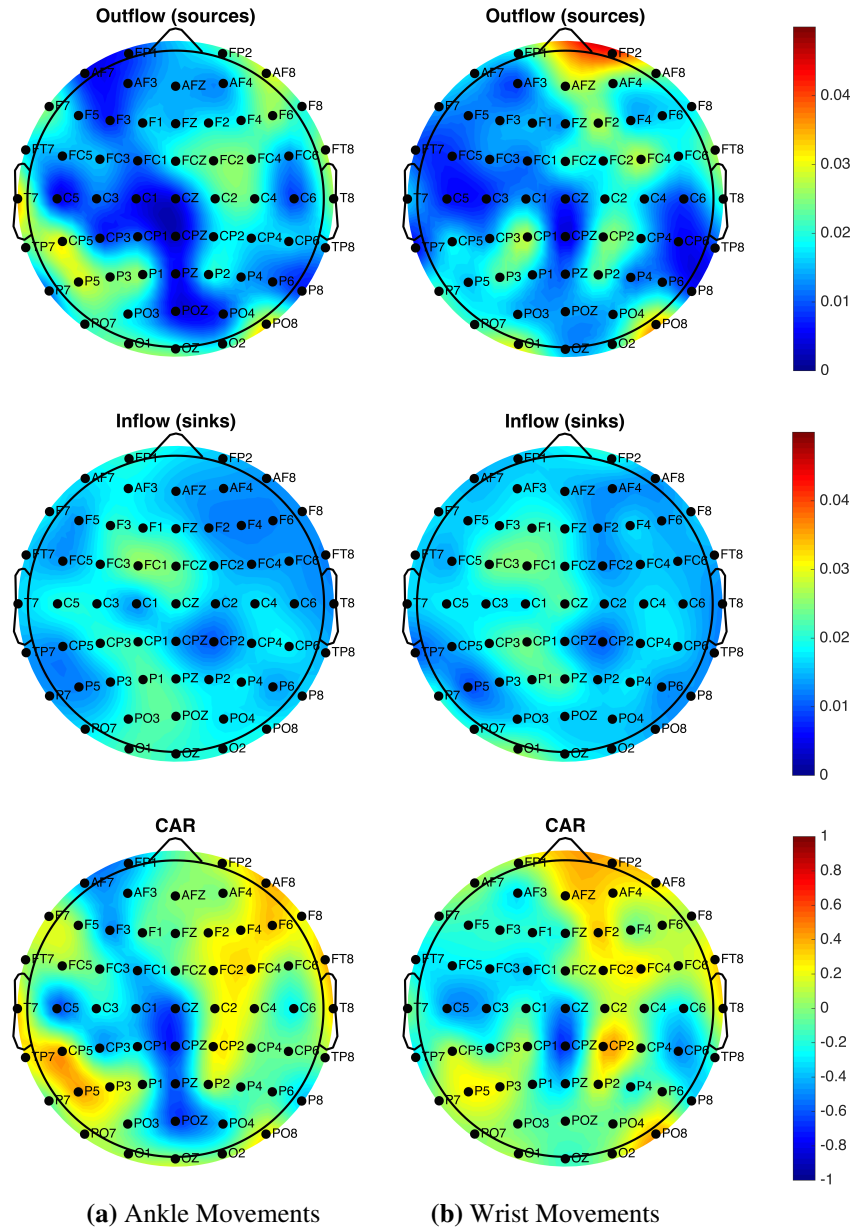


Figure 3.11: Topographical plots showing the static channel-wise graph-theoretical measures calculated on the mean significance matrix during motor tasks. Top: outflow; middle: inflow; bottom: Causal Asymmetry Ratio (CAR).

3.4.2 Dynamic Connectivity Results

As explained before, dynamic or instantaneous connectivity is the result of letting the parameters of the model (and hence the connectivity values) vary adaptively with time. Due to memory limitations, calculation of connectivity parameters from model parameters is done one at a time for small consecutive time windows of 5 seconds. Given the fact that a huge volume of data is generated in this manner, we have resorted to observing only the first 5 seconds of connectivity values in order to see which interactions dominate the connectivity structure at the initial stages of performing a task.

In terms of visualization of the results, all of the Figures in the previous section would turn into videos whose frames depict instantaneous connectivity structures. Naturally, the least detailed and most illustrative videos would be those corresponding to graph-theoretical topographical plots. In Figure 3.12, we have illustrated a few video snapshots from three subjects showing the evolution of the ankle movement connectivity structure throughout the first five-second interval in one-second steps. Shown in the plots is the instantaneous CAR value calculated on gamma band significance matrices obtained from recordings at LSBB.

Alternatively, if the directed interaction between a specific pair of channels $A \rightarrow B$ is of interest, we can plot the time course of the computed connectivity measure (integrated within the gamma band) flowing from A to B . For instance, having identified the major sources (CP2, P5, F4, FC4) and sinks (C3, CP1, CZ, PZ, CP6) of significant gamma band activity for a single subject from plots similar to those in Figure 3.11a, we might be curious to know the specific times at which connections between each of these channels are stronger during ankle movements. Figure 3.13 depicts such information obtained from the first five-second interval of ankle movements from subject 1 at LSBB. The figure illustrates the variability of interactions over time. Specifically, we observe that connections $F4 \rightarrow C3$, $F4 \rightarrow CP1$, and $P5 \rightarrow CZ$ are mainly inactive during this period. Moreover, while $FC4$ is propagating activity only during the initial stages of the task, connections such as $P5 \rightarrow C3$ are activated at later times, and connections $P5 \rightarrow CP1$ and $CP2 \rightarrow CP1$ are consistently active throughout the whole five-second period.

Unfortunately, interpretability of these results and performing a multi-subject

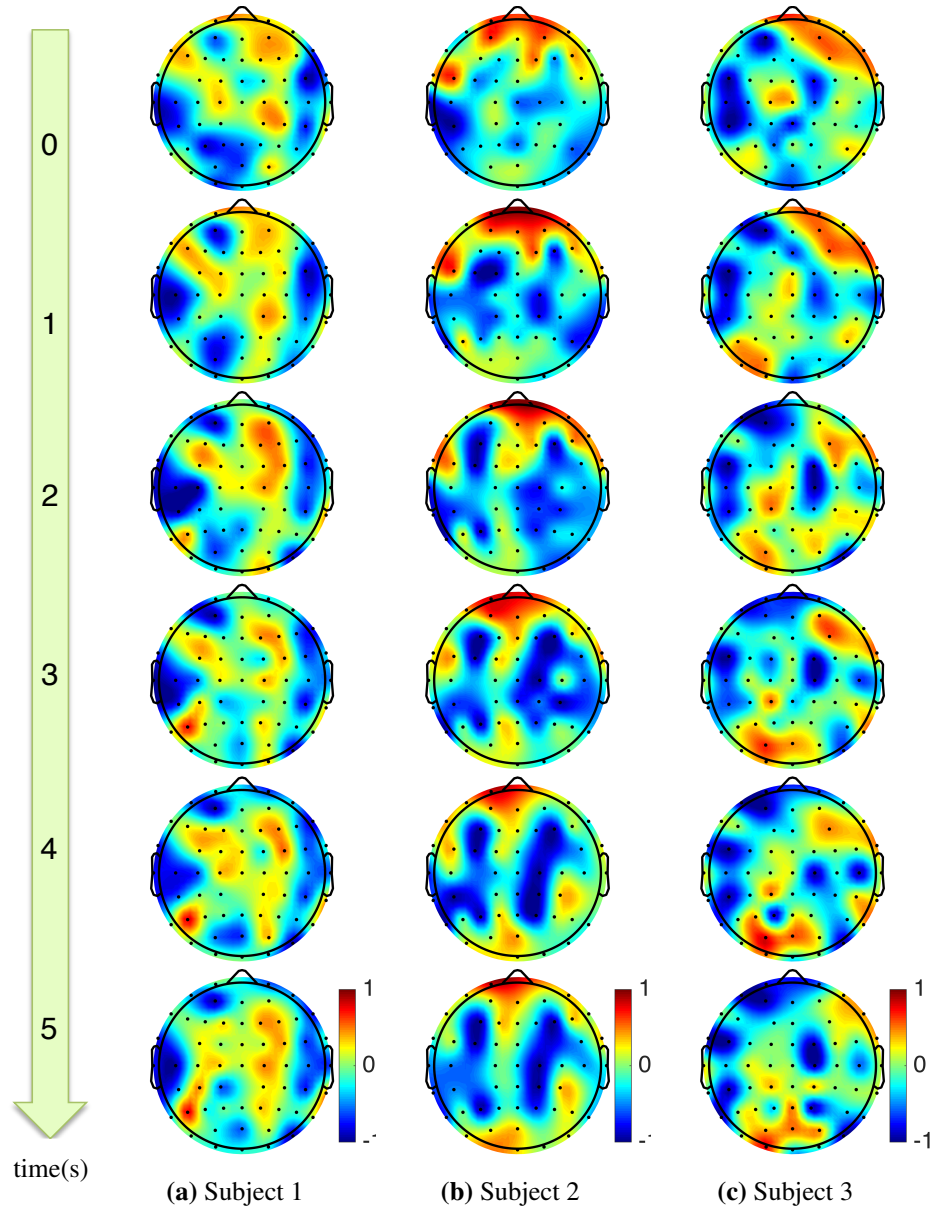


Figure 3.12: Topographical plots of instantaneous significant CAR values during the first five seconds of ankle movement for three subjects in LSBB.

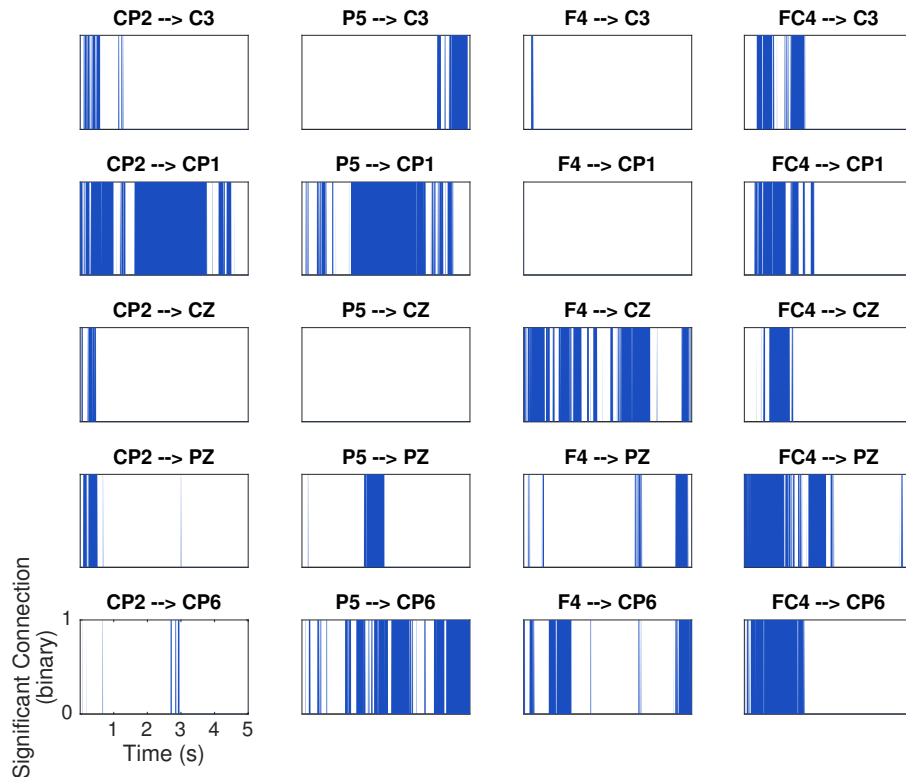


Figure 3.13: Time course of significant gamma band interactions between a selected array of sources and sinks throughout the first five seconds of ankle movement (subject 1, LSBB). Shaded areas represent the presence of significant gamma band interactions across time (horizontal axis).

analysis is severely limited by the protocol definition and design of experiments. It is apparent from Figures 3.12 and 3.13 that the connectivity structure changes rapidly over short instances of time. Hence, in order to be able to compare the time-dependent patterns across subjects and recordings to find consistent connectivity patterns, the movement tasks need to be performed at repeatable epochs, commenced at precisely known start times and executed at closely similar paces. On the contrary, task start times in our dataset were not properly annotated, and the movements were performed at varying self-selected paces. In other words, the subjects in Figure 3.12 are likely in different stages of ankle and wrist movements

due to the high uncertainty in task start times, and hence their activities cannot be compared across time.

3.4.3 Conclusion

Brain connectivity structure comprises networks of different brain sites connected by anatomical, functional, or causal (effective) associations. In this chapter, we extended the segregated analysis of chapter 2 to search for the presence and direction of task-specific gamma band connectivity links in our EEG dataset during motor tasks.

Using the parameters from a data-driven auto-regressive model, we calculated a Granger-causal measure of connectivity, the direct Directed Transfer Function (dDTF), on 10-second segments of the continuous data. This gave rise to a batch-averaged (so-called static) manifestation of the connectivity structure, signifying the general patterns of interaction between channels within the whole batch period. Using the dDTF values obtained from different batches of the same recording, we devised a statistical significance selection procedure based on the distribution of dDTF values across channel pairs, conditions, and subjects in order to distinguish significant connections from insignificant ones. Moreover, to present the high-dimensional results in a compact manner, we introduced graph-theoretical measures of inflow, outflow, and Causal Asymmetry Ratio. The static connectivity results indicated high inter-connectivity across a wide range of brain regions within the gamma band. Hemispherical analysis demonstrated more intra-hemispheric than inter-hemispheric connectivity, and more left-to-right connections than right-to-left (for tasks involving movements of the right hand/ foot). Frontal and central regions contained the most number of significant connections during motor tasks, while significant sources and sinks of information were also seen in other (e.g. parietal) regions.

Furthermore, we extended the auto-regressive model to the adaptive, time-varying case (so-called dynamic connectivity) to incorporate the dimension of time in the analysis. We observed that patterns of connectivity change very rapidly over time, limiting interpretability of the results given the uncertainty of task start times in the current dataset.

Apart from the timing of the experiments, statistical rigor of the results obtained from this dataset is also limited by the small number of participants. More so than any other biological phenomenon, task-specific EEG correlates are known to differ significantly in topology, time-frequency, and connectivity patterns across subjects. Substantial variability was observed even between recordings obtained from the same subject at different times. Hence, many subjects (more than 30, according to the Central Limit Theorem) are needed to obtain more consistent and reliable results, as well as many trials of the same task performed by the same subject. The thorough pipeline and methods introduced in this thesis would be of value to the future studies addressing these limitations.

Chapter 4

Conclusion

4.1 Summary

This thesis was aimed at analysis of high-frequency EEG activity patterns in a dataset consisting of high-dimensional continuous task-specific recordings from a number of subjects in a low-noise environment as well as a typical hospital environment. The analysis was performed both from a segregated and an integrated (connectivity) perspective; with the former investigating isolated channel behaviors and the latter attempting to discern patterns of interaction between different brain sites. Due to its well-suited properties in high frequencies, the Stockwell transform was chosen to reveal gamma band energy enhancements pertaining to specific tasks in the segregated analysis. Using this transform, we analyzed the data from all subjects in search of significant task-specific activity patterns in different frequency bands, and found activity patterns highly dependent on topology (spatial location of the electrode), frequency, and condition (the task being performed). We also used S-Transform to compare the data collected at the low-noise environment with similar data in the hospital environment, and found greater task-relevant gamma band energy increases in LSBB, especially during motor tasks. Based on this observation, the subsequent connectivity analysis was performed solely on motor tasks using a linear, data-driven method based on multivariate Granger causality. A rigorous framework for block-averaged as well as instantaneous connectivity analysis was proposed and implemented on the data. Block-averaged connectivity analysis

revealed well-defined patterns during ankle and wrist movements, possibly valuable for further neurological analysis if more subjects are included in the study. On the other hand, unrepeatability of task-specific epochs, resulting from the lack of time-locked task performances, limited the multi-subject analysis of instantaneous connectivity patterns.

4.2 Limitations

This work was limited by a number of issues stemming from imperfections in data collection, most notably lack of precisely annotated data. To elaborate, the data was continuously recorded in the NRSign software with annotations denoting start and end times of different phases of the experiment (e.g. onset of a counting epoch immediately following rest). These annotations were manually added online, giving rise to human errors in orders of seconds which increase with increasing recording time. Moreover, the alternating epochs of rest/task in LSBB were not annotated at all. As a case in point, a two-minute recording of backward counting consists of two episodes of a 30-second counting epoch followed by 30 seconds of rest; whereas the annotations in LSBB denoted the whole two minutes as counting, leaving the onsets of resting epochs unknown. This was an issue because despite the efforts to keep the duration of epochs fixed at 30 seconds, examining the annotated epochs at ICORD showed that in some cases the length of each rest/task epoch differed from 30 seconds by a few seconds. Due to lack of annotations at LSBB, in this thesis we have regarded the mixed task-and-rest recordings (such as the count-and-rest recording described above) as task recordings, comparing them with resting-state recordings which we knew for sure corresponded to the resting condition. The reasoning behind this approach was that if the gamma band energy is increased during a task, more gamma band energy would be present in a task-and-rest recording than in a recording solely comprising of resting-state data. However, we acknowledge that this procedure might obscure some task-specific features and make baseline comparisons difficult, as well as compromise on task-rest statistical significance results.

Furthermore, while the focus of our study was on continuous gamma band oscillations in relatively long periods of time, most studies of cognitive and sensory

gamma band correlates were performed in an induced (e.g. ERP) framework with time-locked stimuli. This might be the reason why no major task-specific gamma band increases were observed during cognitive and sensory tasks in section 2.3.2. Time-locked experiments with proper annotation schemes, such as auditory cues with automated timing, could be important and valuable to examine in future work.

Another limitation in the dataset was the fact that the number of uncontaminated channels differed between subjects, recordings and environments. While in some cases two or three channels were rejected due to artifacts for one subject, as many as ten channels were rejected for another subject. This could have obscured important information and biased the results, especially during identification of sources and sinks in connectivity analysis. This issue is also the main reason why a comparative analysis of connectivity structures in ICORD and LSBB was not performed, since the artifactual channels rejected from subjects' recordings differed in the two environments.

On a different note, choosing the prefrontal electrode FPZ as the reference electrode might not have been the safest choice in that it causes blink and eye movement artifacts to appear in all other electrodes. While the data can be easily re-referenced offline for segregated analysis, re-referencing is not an option for connectivity analysis since it introduces false inter-relations between channels. Generally, ear lobes (averaged mastoids) might be a safer choice for positioning the reference electrodes and mitigation of blink artifacts, since they record activity which is not drastically different from other electrodes while recording less brain activity.

4.3 Future Work

Future improvement efforts can be twofold: 1) efforts to address the limitations of the current study protocol (inclusion of more subjects, precise data annotations, and time-locked experiments, as well as online data monitoring from time to time to ensure quality of all recording electrodes); and 2) efforts to improve the data analysis framework, including but not limited to:

- use of more rigorous statistical testing methods, such as mixed-model designs, repeated measures ANOVA, permutation testing and bootstrap,

- use of machine learning and Markovian models in dynamic connectivity to examine potentially consistent patterns (e.g. two regions following each other consistently but in a transient fashion),
- including nonlinear analysis methods (entropy, measures of signal complexity, mutual information),
- inclusion of more abstract graph-theoretical measures (such as path length, global efficiency, and measures of centrality and modularity) and their task-specific correlates.

These methods will be inspected for feasibility and implemented in future publications. Future work will also include static connectivity analysis in other tasks and other frequency bands.

Bibliography

- [1] M Brazier. The eeg in epilepsy a historical note. *Epilepsia*, 1(1-5):328–336, 1959. → pages 1
- [2] E Niedermeyer and F da Silva. *Electroencephalography: basic principles, clinical applications, and related fields*. Lippincott Williams & Wilkins, 2005. → pages 1
- [3] H Schwilden, J Schüttler, and H Stoeckel. Closed-loop feedback control of methohexital anesthesia by quantitative eeg analysis in humans. *Anesthesiology*, 67(3):341–347, 1987. → pages 1
- [4] J Wolpaw, N Birbaumer, W Heetderks, D McFarland, P Peckham, G Schalk, E Donchin, L Quatrano, C Robinson, T Vaughan, et al. Brain-computer interface technology: a review of the first international meeting. *IEEE transactions on rehabilitation engineering*, 8(2):164–173, 2000. → pages 1
- [5] J Cacioppo, L Tassinary, and G Berntson. *Handbook of psychophysiology*. Cambridge University Press, 2007. → pages 1, 5, 14
- [6] J Tao, A Ray, S Hawes-Ebersole, and J Ebersole. Intracranial eeg substrates of scalp eeg interictal spikes. *Epilepsia*, 46(5):669–676, 2005. → pages 3
- [7] G Buzsaki. *Rhythms of the Brain*. Oxford University Press, 2006. → pages 3
- [8] C Herrmann, M Munk, and A Engel. Cognitive functions of gamma-band activity: memory match and utilization. *Trends in cognitive sciences*, 8(8):347–355, 2004. → pages 5
- [9] C Gray, P König, A Engel, W Singer, et al. Oscillatory responses in cat visual cortex exhibit inter-columnar synchronization which reflects global stimulus properties. *Nature*, 338(6213):334–337, 1989. → pages 5

- [10] H Tiitinen, J Sinkkonen, K Reinikainen, K Alho, J Lavikainen, and R Näätänen. Selective attention enhances the auditory 40-hz transient response in humans. 1993. → pages 5
- [11] D Strüber, C Basar-Eroglu, E Hoff, and M Stadler. Reversal-rate dependent differences in the eeg gamma-band during multistable visual perception. *International Journal of Psychophysiology*, 38(3):243–252, 2000. → pages 5
- [12] O Jensen, J Kaiser, and J Lachaux. Human gamma-frequency oscillations associated with attention and memory. *Trends in neurosciences*, 30(7):317–324, 2007. → pages 5
- [13] E Başar, C Başar-Eroğlu, S Karakaş, and M Schürmann. Brain oscillations in perception and memory. *International journal of psychophysiology*, 35(2):95–124, 2000. → pages 5
- [14] F Pulvermüller, N Birbaumer, W Lutzenberger, and B Mohr. High-frequency brain activity: its possible role in attention, perception and language processing. *Progress in neurobiology*, 52(5):427–445, 1997. → pages 5
- [15] A Engel, P Fries, and W Singer. Dynamic predictions: oscillations and synchrony in top–down processing. *Nature Reviews Neuroscience*, 2(10):704–716, 2001. → pages 5
- [16] D Cheyne, S Bells, P Ferrari, W Gaetz, and A Bostan. Self-paced movements induce high-frequency gamma oscillations in primary motor cortex. *Neuroimage*, 42(1):332–342, 2008. → pages 5
- [17] Z Zhang, L Hu, Y Hung, A Mouraux, and G Iannetti. Gamma-band oscillations in the primary somatosensory cortex: direct and obligatory correlate of subjective pain intensity. *The Journal of Neuroscience*, 32(22):7429–7438, 2012. → pages 5, 27
- [18] R Galambos. A comparison of certain gamma band (40-hz) brain rhythms in cat and man. In *Induced rhythms in the brain*, pages 201–216. Springer, 1992. → pages 5
- [19] D Subha, P Joseph, R Acharya, and C Lim. Eeg signal analysis: a survey. *Journal of medical systems*, 34(2):195–212, 2010. → pages 6
- [20] S Sanei and J Chambers. *EEG signal processing*. John Wiley & Sons, 2013. → pages 6

- [21] L Sörnmo and P Laguna. *Bioelectrical signal processing in cardiac and neurological applications*, volume 8. Academic Press, 2005. → pages 6
- [22] B Hjorth. Eeg analysis based on time domain properties. *Electroencephalography and clinical neurophysiology*, 29(3):306–310, 1970. → pages 6
- [23] A Luo and T Sullivan. A user-friendly ssvep-based brain–computer interface using a time-domain classifier. *Journal of neural engineering*, 7(2):026010, 2010. → pages 6
- [24] O Faust, R Acharya, L Min, and B Spath. Automatic identification of epileptic and background eeg signals using frequency domain parameters. *International journal of neural systems*, 20(02):159–176, 2010. → pages 6
- [25] P Valdés, J Bosch, R Grave, J Hernandez, J Riera, R Pascual, and R Biscay. Frequency domain models of the eeg. *Brain topography*, 4(4):309–319, 1992. → pages 6
- [26] S Blanco, A Figliola, R Quian Quiroga, OA Rosso, and E Serrano. Time-frequency analysis of electroencephalogram series. iii. wavelet packets and information cost function. *Physical Review E*, 57(1):932, 1998. → pages 6
- [27] S Qian and D Chen. Joint time-frequency analysis. *IEEE Signal Processing Magazine*, 16(2):52–67, 1999. → pages 6
- [28] N Ince, S Arica, and A Tewfik. Classification of single trial motor imagery eeg recordings with subject adapted non-dyadic arbitrary time–frequency tilings. *Journal of neural engineering*, 3(3):235, 2006. → pages 6
- [29] B Graimann and G Pfurtscheller. Quantification and visualization of event-related changes in oscillatory brain activity in the time–frequency domain. *Progress in brain research*, 159:79–97, 2006. → pages 6
- [30] J Jeong, J Gore, and B Peterson. Mutual information analysis of the eeg in patients with alzheimer’s disease. *Clinical Neurophysiology*, 112(5):827–835, 2001. → pages 6
- [31] J Muthuswamy, D Sherman, and N Thakor. Higher-order spectral analysis of burst patterns in eeg. *IEEE Transactions on Biomedical Engineering*, 46(1):92–99, 1999. → pages 6

- [32] R Acharya, E Chua, K Chua, L Min, and T Tamura. Analysis and automatic identification of sleep stages using higher order spectra. *International journal of neural systems*, 20(06):509–521, 2010. → pages 6
- [33] E Pereda, A Gamundi, R Rial, and J González. Non-linear behaviour of human eeg: fractal exponent versus correlation dimension in awake and sleep stages. *Neuroscience letters*, 250(2):91–94, 1998. → pages 6
- [34] C Stam. Nonlinear dynamical analysis of eeg and meg: review of an emerging field. *Clinical Neurophysiology*, 116(10):2266–2301, 2005. → pages 6
- [35] D Abásolo, R Hornero, P Espino, D Alvarez, and J Poza. Entropy analysis of the eeg background activity in alzheimer’s disease patients. *Physiological measurement*, 27(3):241, 2006. → pages 6
- [36] N Kannathal, M Choo, R Acharya, and P Sadasivan. Entropies for detection of epilepsy in eeg. *Computer methods and programs in biomedicine*, 80(3):187–194, 2005. → pages 6
- [37] R Grech, T Cassar, J Muscat, K Camilleri, S Fabri, M Zervakis, P Xanthopoulos, V Sakkalis, and B Vanrumste. Review on solving the inverse problem in eeg source analysis. *Journal of neuroengineering and rehabilitation*, 5(1):1, 2008. → pages 6
- [38] R Pascual-Marqui. Review of methods for solving the eeg inverse problem. *International journal of bioelectromagnetism*, 1(1):75–86, 1999. → pages 6
- [39] B Cuffin. Eeg dipole source localization. *IEEE engineering in medicine and biology magazine*, 17(5):118–122, 1998. → pages 7
- [40] M Hämäläinen and R Ilmoniemi. Interpreting magnetic fields of the brain: minimum norm estimates. *Medical & biological engineering & computing*, 32(1):35–42, 1994. → pages 7
- [41] R Pascual-Marqui, C Michel, and D Lehmann. Low resolution electromagnetic tomography: a new method for localizing electrical activity in the brain. *International Journal of psychophysiology*, 18(1):49–65, 1994. → pages 7
- [42] S Baillet and L Garnero. A bayesian approach to introducing anatomic-functional priors in the eeg/meg inverse problem. *IEEE transactions on Biomedical Engineering*, 44(5):374–385, 1997. → pages 7

- [43] S Makeig, A Bell, T Jung, T Sejnowski, et al. Independent component analysis of electroencephalographic data. *Advances in neural information processing systems*, pages 145–151, 1996. → pages 7
- [44] V Sakkalis. Review of advanced techniques for the estimation of brain connectivity measured with eeg/meg. *Computers in biology and medicine*, 41(12):1110–1117, 2011. → pages 7
- [45] J Schoffelen and J Gross. Source connectivity analysis with meg and eeg. *Human brain mapping*, 30(6):1857–1865, 2009. → pages 7
- [46] J Damoiseaux and M Greicius. Greater than the sum of its parts: a review of studies combining structural connectivity and resting-state functional connectivity. *Brain Structure and Function*, 213(6):525–533, 2009. → pages 7
- [47] J Peters, M Taquet, C Vega, S Jeste, I Fernández, J Tan, C Nelson, M Sahin, and S Warfield. Brain functional networks in syndromic and non-syndromic autism: a graph theoretical study of eeg connectivity. *BMC medicine*, 11(1):54, 2013. → pages 7
- [48] K Blinowska. Review of the methods of determination of directed connectivity from multichannel data. *Medical & biological engineering & computing*, 49(5):521–529, 2011. → pages 7, 42
- [49] K Friston, L Harrison, and W Penny. Dynamic causal modelling. *Neuroimage*, 19(4):1273–1302, 2003. → pages 7, 41
- [50] W Penny, K Stephan, A Mechelli, and K Friston. Modelling functional integration: a comparison of structural equation and dynamic causal models. *Neuroimage*, 23:S264–S274, 2004. → pages 7, 41
- [51] A Schlögl and G Supp. Analyzing event-related eeg data with multivariate autoregressive parameters. *Progress in brain research*, 159:135–147, 2006. → pages 7, 52
- [52] A Zandi, G Dumont, M Yedlin, P Lapeyrie, C Sudre, and S Gaffet. Scalp eeg acquisition in a low-noise environment: A quantitative assessment. *IEEE Transactions on Biomedical Engineering*, 58(8):2407–2417, 2011. → pages 8, 27
- [53] R Stockwell, L Mansinha, and R Lowe. Localization of the complex spectrum: the s transform. *IEEE transactions on signal processing*, 44(4):998–1001, 1996. → pages 8, 19

- [54] K Kirschfeld. The physical basis of alpha waves in the electroencephalogram and the origin of the berger effect. *Biological cybernetics*, 92(3):177–185, 2005. → pages 11
- [55] J Polich and A Kok. Cognitive and biological determinants of p300: an integrative review. *Biological psychology*, 41(2):103–146, 1995. → pages 12
- [56] G Pfurtscheller. Eeg rhythms-event-related desynchronization and synchronization. In *Rhythms in Physiological systems*, pages 289–296. Springer, 1991. → pages 12
- [57] G Pfurtscheller, K Pichler-Zalaudek, and C Neuper. Erd and ers in voluntary movement of different limbs. *Event-related desynchronization handbook of electroencephalography and clinical neurophysiology. Volume, 6*, 1999. → pages 12
- [58] W Singer. Synchronization of cortical activity and its putative role in information processing and learning. *Annual review of physiology*, 55(1):349–374, 1993. → pages 12
- [59] J Urigüen and B Garcia-Zapirain. Eeg artifact removalstate-of-the-art and guidelines. *Journal of neural engineering*, 12(3):031001, 2015. → pages 14
- [60] P He, G Wilson, and C Russell. Removal of ocular artifacts from electro-encephalogram by adaptive filtering. *Medical and biological engineering and computing*, 42(3):407–412, 2004. → pages 14
- [61] C James and C Hesse. Independent component analysis for biomedical signals. *Physiological measurement*, 26(1):R15, 2004. → pages 14
- [62] M Uusitalo and R Ilmoniemi. Signal-space projection method for separating meg or eeg into components. *Medical and Biological Engineering and Computing*, 35(2):135–140, 1997. → pages 14
- [63] M Unser and A Aldroubi. A review of wavelets in biomedical applications. *Proceedings of the IEEE*, 84(4):626–638, 1996. → pages 14
- [64] T Jung, S Makeig, C Humphries, T Lee, M Mckeown, V Iragui, and T Sejnowski. Removing electroencephalographic artifacts by blind source separation. *Psychophysiology*, 37(2):163–178, 2000. → pages 14, 16

- [65] A Delorme and S Makeig. Eeglab: an open source toolbox for analysis of single-trial eeg dynamics including independent component analysis. *Journal of neuroscience methods*, 134(1):9–21, 2004. → pages 16
- [66] J Onton and S Makeig. Information-based modeling of event-related brain dynamics. *Progress in brain research*, 159:99–120, 2006. → pages 16
- [67] R Stockwell. Why use the s-transform. *AMS Pseudo-differential operators: Partial differential equations and time-frequency analysis*, 52:279–309, 2007. → pages 19, 20
- [68] G Tononi, O Sporns, and G Edelman. A measure for brain complexity: relating functional segregation and integration in the nervous system. *Proceedings of the National Academy of Sciences*, 91(11):5033–5037, 1994. → pages 39
- [69] S Finger. *Origins of neuroscience: a history of explorations into brain function*. Oxford University Press, USA, 2001. → pages 39
- [70] V Calhoun, R Miller, G Pearlson, and T Adalı. The chronnectome: time-varying connectivity networks as the next frontier in fmri data discovery. *Neuron*, 84(2):262–274, 2014. → pages 39
- [71] A Eklund, T Nichols, and H Knutsson. Cluster failure: Why fmri inferences for spatial extent have inflated false-positive rates. *Proceedings of the National Academy of Sciences*, page 201602413, 2016. → pages 40
- [72] F Wouterlood, M Vinkenoog, and M van den Oever. Tracing tools to resolve neural circuits. *Network: Computation in Neural Systems*, 13(3):327–342, 2002. → pages 40
- [73] G Gong, Y He, L Concha, C Lebel, D Gross, A Evans, and C Beaulieu. Mapping anatomical connectivity patterns of human cerebral cortex using in vivo diffusion tensor imaging tractography. *Cerebral cortex*, 19(3):524–536, 2009. → pages 40
- [74] M Hutchison, T Womelsdorf, E Allen, P Bandettini, V Calhoun, M Corbetta, S Della Penna, J Duyn, G Glover, J Gonzalez-Castillo, et al. Dynamic functional connectivity: promise, issues, and interpretations. *Neuroimage*, 80:360–378, 2013. → pages 40, 43
- [75] K Friston. Functional and effective connectivity: a review. *Brain connectivity*, 1(1):13–36, 2011. → pages 41

- [76] A Protzner and A McIntosh. Testing effective connectivity changes with structural equation modeling: what does a bad model tell us? *Human brain mapping*, 27(12):935–947, 2006. → pages 41
- [77] R Vicente, M Wibral, M Lindner, and G Pipa. Transfer entropy a model-free measure of effective connectivity for the neurosciences. *Journal of computational neuroscience*, 30(1):45–67, 2011. → pages 41
- [78] Z Wang, P Lee, and M McKeown. A novel segmentation, mutual information network framework for eeg analysis of motor tasks. *Biomedical engineering online*, 8(1):1, 2009. → pages 41
- [79] G Nolte, O Bai, L Wheaton, Z Mari, S Vorbach, and M Hallett. Identifying true brain interaction from eeg data using the imaginary part of coherency. *Clinical neurophysiology*, 115(10):2292–2307, 2004. → pages 42
- [80] A Bastos and J Schoffelen. A tutorial review of functional connectivity analysis methods and their interpretational pitfalls. *Frontiers in systems neuroscience*, 9, 2015. → pages 42
- [81] K Blinowska and M Malinowski. Non-linear and linear forecasting of the eeg time series. *Biological cybernetics*, 66(2):159–165, 1991. → pages 42
- [82] C Granger. Investigating causal relations by econometric models and cross-spectral methods. *Econometrica: Journal of the Econometric Society*, pages 424–438, 1969. → pages 42, 43
- [83] S Bressler and A Seth. Wiener–granger causality: a well established methodology. *Neuroimage*, 58(2):323–329, 2011. → pages 42
- [84] M Kaminski and K Blinowska. A new method of the description of the information flow in the brain structures. *Biological cybernetics*, 65(3):203–210, 1991. → pages 42, 48
- [85] M Centeno and D Carmichael. Network connectivity in epilepsy: resting state fmri and eeg–fmri contributions. *Frontiers in neurology*, 5:93, 2014. → pages 43
- [86] M Eichler. On the evaluation of information flow in multivariate systems by the directed transfer function. *Biological cybernetics*, 94(6):469–482, 2006. → pages 45, 49
- [87] H Lütkepohl. *New introduction to multiple time series analysis*. Springer Science & Business Media, 2005. → pages 45

- [88] S Chennu, P Finoia, E Kamau, J Allanson, G Williams, M Monti, V Noreika, A Arnatkeviciute, A Canales-Johnson, F Olivares, et al. Spectral signatures of reorganised brain networks in disorders of consciousness. *PLoS Comput Biol*, 10(10):e1003887, 2014. → pages 45, 52
- [89] M Kamiński, K Blinowska, and W Szelenberger. Topographic analysis of coherence and propagation of eeg activity during sleep and wakefulness. *Electroencephalography and clinical neurophysiology*, 102(3):216–227, 1997. → pages 45, 52
- [90] Y Saito and H Harashima. Tracking of information within multichannel {EEG} record causal analysis in {EEG}. Yamaguchi N, Fujisawa K (eds) *Recent advances in {EEG} and {EMG} data processing*. Elsevier, pages 133–146, 1981. → pages 48
- [91] L Astolfi, F Cincotti, D Mattia, C Babiloni, F Carducci, A Basilisco, P Rossini, S Salinari, L Ding, Y Ni, et al. Assessing cortical functional connectivity by linear inverse estimation and directed transfer function: simulations and application to real data. *Clinical neurophysiology*, 116(4):920–932, 2005. → pages 48
- [92] J Rosenberg, D Halliday, P Breeze, and B Conway. Identification of patterns of neuronal connectivity: partial spectra, partial coherence, and neuronal interactions. *Journal of neuroscience methods*, 83(1):57–72, 1998. → pages 48
- [93] D Bringer. Time series: Data analysis and theory. *Expanded Edition*, HoldenDay, 1981. → pages 48
- [94] V Jirsa and A McIntosh. *Handbook of brain connectivity*, volume 1. Springer, 2007. → pages 48
- [95] L Baccalá and K Sameshima. Partial directed coherence: a new concept in neural structure determination. *Biological cybernetics*, 84(6):463–474, 2001. → pages 48
- [96] K Sameshima and L Baccalá. Using partial directed coherence to describe neuronal ensemble interactions. *Journal of neuroscience methods*, 94(1):93–103, 1999. → pages 48
- [97] L Astolfi and F Babiloni. Estimation of cortical connectivity in humans: Advanced signal processing techniques. *Synthesis Lectures on Biomedical Engineering*, 2(1):1–95, 2007. → pages 49

- [98] A Korzeniewska, M Mańczak, M Kamiński, K Blinowska, and S Kasicki. Determination of information flow direction among brain structures by a modified directed transfer function (ddtf) method. *Journal of neuroscience methods*, 125(1):195–207, 2003. → pages 49
- [99] L Astolfi, F Cincotti, D Mattia, M Marciani, L Baccala, F de Vico Fallani, S Salinari, M Ursino, M Zavaglia, L Ding, et al. Comparison of different cortical connectivity estimators for high-resolution eeg recordings. *Human brain mapping*, 28(2):143–157, 2007. → pages 50
- [100] F Chella, V Pizzella, F Zappasodi, and L Marzetti. Impact of the reference choice on scalp eeg connectivity estimation. *Journal of neural engineering*, 13(3):036016, 2016. → pages 51
- [101] A Neumaier and T Schneider. Estimation of parameters and eigenmodes of multivariate autoregressive models. *ACM Transactions on Mathematical Software (TOMS)*, 27(1):27–57, 2001. → pages 52
- [102] T Schneider and A Neumaier. Algorithm 808: Arfit matlab package for the estimation of parameters and eigenmodes of multivariate autoregressive models. *ACM Transactions on Mathematical Software (TOMS)*, 27(1):58–65, 2001. → pages 52
- [103] E Möller, B Schack, M Arnold, and H Witte. Instantaneous multivariate eeg coherence analysis by means of adaptive high-dimensional autoregressive models. *Journal of neuroscience methods*, 105(2):143–158, 2001. → pages 53
- [104] H Akaike. Fitting autoregressive models for prediction. *Annals of the institute of Statistical Mathematics*, 21(1):243–247, 1969. → pages 53
- [105] G Schwarz et al. Estimating the dimension of a model. *The annals of statistics*, 6(2):461–464, 1978. → pages 53
- [106] M Rubinov and O Sporns. Complex network measures of brain connectivity: uses and interpretations. *Neuroimage*, 52(3):1059–1069, 2010. → pages 61
- [107] T Mullen, Z Acar, G Worrell, and S Makeig. Modeling cortical source dynamics and interactions during seizure. In *2011 Annual International Conference of the IEEE Engineering in Medicine and Biology Society*, pages 1411–1414. IEEE, 2011. → pages 61

- [108] F Roux, M Wibral, H Mohr, W Singer, and P Uhlhaas. Gamma-band activity in human prefrontal cortex codes for the number of relevant items maintained in working memory. *Journal of Neuroscience*, 32(36):12411–12420, 2012. → pages 69
- [109] G Waysand, S Gaffet, J Virieux, A Chwala, M Auguste, D Boyer, A Cavaillou, Y Guglielmi, and D Rodrigues. The laboratoire souterrain bas bruit (lsbb) in rustrel-pays d’apt (france): A unique opportunity for low-noise underground science. In *EGS General Assembly Conference Abstracts*, volume 27, page 3869, 2002. → pages 91

Appendix A

Details of the Study

A.1 The Underground Facility

The Laboratoire Souterrain à Bas Bruit (LSBB) is a unique low-noise facility under the karstic Lubéron plateau in Rustrel, France. Formerly used as a ground based component of the French nuclear missile system, this underground capsule is robust to radioactive clouds, thermal and mechanical waves and electromagnetic interference, and has now been progressively used as a cross disciplinary laboratory. The 28×8 meter capsule is located 500 meters underground and is surrounded by 1 *cm* of steel in addition to 2 *m* of reinforced concrete, thus being a completely shielded Faraday cage with a residual electromagnetic noise lower than 2 fT/Hz above 10 *Hz* [109]. The absence of sources of electromagnetic interference makes LSBB an ideal environment for performing low-noise measurements of physiological signals such as EEG, particularly in frequencies above 30 *Hz* which are specifically susceptible to high-frequency noise.

A.2 Acquisition System

In this project, we have used a research-grade EEG system ¹ capable of non-invasive acquisition of scalp EEG. The system works on battery and has 64 chan-

¹NR SIGN EEG 5000Q 64-channel (NR SIGN Inc., New Westminster, BC, Canada), <http://www.nrsign.com/eeg/eeg-5000q>

nels² (see Fig. A.1), thus offering considerably higher spatial resolution for the scalp potentials than the previous two-channel system. The system allows for a programmable sample rate of 500 Hz to 2 KHz with resolution of 16 bits. Due to acquiring progressively longer data segments and limitations faced in storing the data, the sampling rate was fixed at 500 Hz. Data was transferred using a USB cable to a laptop computer (also running on battery power) through the NR SIGN EEG application software. The raw data was then exported to MATLAB (R2015b) in an offline procedure for quantitative analysis.

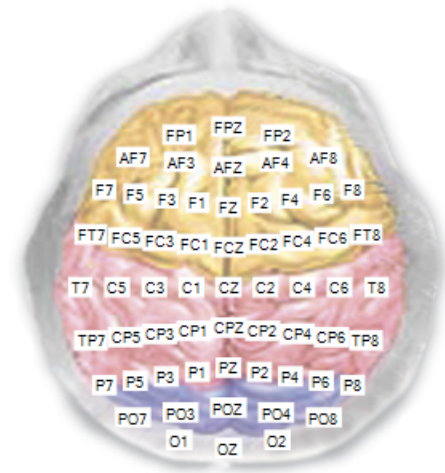


Figure A.1: EEG montage of the NRSign acquisition system. The 1cm surface scalp electrodes are placed as per the 10-10 international EEG system (higher density of electrodes than the 10-20 system shown in Fig 1.1) for standardized reproducibility.

A.3 Study Protocol

EEG was first acquired using the above system in the LSBB capsule. For comparison purposes, the same equipment and recording protocol was then used to acquire

² There were 60 actual channels recording meaningful data out of the total 64 channels in the system: two channels are implemented for recording surface EMG (Electromyogram), one channel is used for recording ECG (these channels are usually helpful in epilepsy applications and hence, they were not set to record data in our experimental paradigm), and channel FPZ was used as the reference electrode (set to zero at all times). The ground electrode was placed on the wrist.

control recordings at a hospital environment (the International Collaboration On Repair Discoveries (ICORD) in Vancouver General Hospital).

Seven subjects (three females) varying in age from early thirties to early sixties participated in data acquisition at LSBB in France; while five subjects (two females) participated in the acquisition at ICORD in Vancouver. All subjects were right-hand dominant. Due to the logistically challenging nature of taking replicate recordings on different continents, only four subjects (two females) were common to both environments.

During a recording period at either LSBB or the hospital environment, subjects performed a number of cognitive, sensory, and motor tasks with ample time between experiments so that each subject was rested, comfortable, and ready to move on to the next task. Each five-hour recording period consisted of the following phases:

1. Resting state EEG:

The subjects were placed supine in a darkened room, lying as still as possible while EEG was being recorded for seven minutes. The subjects were asked to open/close their eyes every 30 seconds for five minutes, and keep their eyes closed during the last two minutes.

2. Cognitive EEG:

(a) **Counting** - With eyes closed, the subjects counted backwards for four 30-second periods with 30-second periods of rest in between (total counting period of two minutes). Counting started from some large randomly selected number and decremented by 7 or 6 at each step.

(b) **Matching** - Subjects then performed an increasingly challenging memory task on an iPad which required recalling and matching the location of identically-shaped objects. Similarly to the counting task, matching was performed for two minutes (four 30-second intervals) with two minutes (four 30-second intervals) of rest in between.

3. EEG during pain and sensory stimulation:

- (a) **Light touch (brushing)** - As an innocuous tactile stimulus, a cotton swab was used to 'brush' the adductor pollicis region (proximal joint of thumb) of the right hand. Brushing was performed at a constant rate (~2 Hz) for five minutes, during which the subjects opened and closed their eyes in ten alternating 30-second intervals.
- (b) **Noxious EEG (heat)** - First, skin temperature was measured by application of a temperature sensor to the skin surface for a period of 1 minute. Consequently, as a noxious tactile stimulation phenomenon, hot packs were applied to the adductor pollicis region for five minutes, with 30-second periods alternating between eyes-open and eyes-closed conditions. At the end of each 30-second period, the subjects rated the intensity of their perceived pain based on a (0-10, 10 being the most painful) visual analog scale (VAS). Finally, skin temperature over the adductor pollicis was measured and recorded again to evaluate the effect of the heat pack.

4. EEG during motor function:

- (a) **Ankle movements** - Subjects performed reciprocal dorsal and plantar flexion movements of the right ankle for five minutes, with 30 seconds of movement alternating with 30 seconds of rest. Movements were performed with closed eyes at a self-selected speed (~1.5 Hz) and subjects were asked to silently count and report the total number of movements at the end of each 30-second movement period.
- (b) **Wrist movements** - Subjects performed repeated upwards flexion and extension movements of the right wrist (fingers held straight) for five minutes, with alternating 3-second periods of rest in between. Movements were performed with closed eyes at a self-selected pace (~1.5 Hz) and subjects were asked to silently count and report the total number of movements at the end of each 30-second movement period.